Experimental Study of Disruption of Columnar Grain Growth during Rapid Solidification

By

Bharat Yelamanchi

Submitted in Partial Fulfillment of the Requirements

for the Degree of

Masters of Science

in the

Industrial and Systems Engineering

Program

YOUNGSTOWN STATE UNIVERSITY

August 2015

Experimental Study of Disruption of Columnar Grain Growth during Rapid Solidification

By

Bharat Yelamanchi

I hereby release this thesis to the public. I understand that this thesis will be made available from the OhioLINK ETD Center and the Maag Library Circulation Desk for public access. I also authorize the University or other individuals to make copies of this thesis as needed for scholarly research.

Signature:

Bharat Yelamanchi, Student Date

Approvals:

Dr. Guha P. Manogharan, Thesis Advisor Date

Dr. Brett P. Conner, Committee Member Date

Dr. Darrell R. Wallace, Committee Member Date

Dr. Salvatore A. Sanders, Associate Dean of Graduate Studies Date

ABSTRACT

Over the years, many studies have been conducted to study and analyze the grain structures of metal alloys in order for them to have superior structural and mechanical properties. In particular, columnar grains are observed predominantly during rapid solidification of molten metal. This leads to lower mechanical properties and requires expensive secondary heat-treatment processes. This study is aimed at disrupting the formation of columnar grain growth during rapid solidification using ultrasonic vibration and analyzes the effects on grain structure and mechanical properties. A MIG welder mounted on a low cost metal 3D printer was used to deposit ER70S-6 mild steel layers on a plate. A contact type ultrasonic transducer with control system to vary the frequency and power of the vibration was used. The effects of ultrasonic vibration were determined from the statistical analysis of microstructure using ImageJ and micro-indentation techniques on the deposited layer and heat affected zone. It was found that both frequency and interaction between frequency and power had significant impact on the refinement of average grain size up to 10.64% and increased the number of grains by approximately 41.78%. Analysis of micro-indentation tests showed that there was an increase of approximately 14.3% in micro-hardness and 35.77% in Young's modulus due to the applied frequency during rapid solidification. Along with the results from this study, further efforts in modeling and experimentation of multi directional vibrations would lead to a better understanding of disrupting columnar grains in applications that use mechanical vibrations, such as welding, metal additive manufacturing, brazing, and the likes.

Acknowledgements

I would like to express my sincere and deepest gratitude to my advisor Dr. Guha P. Manogharan for providing constant motivation and support to have a wonderful learning curve. Also I would like to thank Dr. Hazel Marie and my committee members Dr. Brett P. Conner and Dr. Darrell R. Wallace for providing valuable feedbacks for completion of this work.

I would like to thank James cook for help with the transducer driver, John Dodson for machining the printer parts, “The Grad. Guys”; i.e. Kyle Myers, Mike Juhasz, George Kubas and Matt Caputo for providing moral and technical assistance, Liseli Baich for help with operation of 3D printer, Sanjay Shrestha for help with sample preparation, Ram A Gullapalli and Karen A. Schilling for help with data collection and a special thanks to Dr. Virgil C Solomon for providing valuable suggestions for sample preparation, microstructure analysis.

Finally I would like to thank my parents for their constant support, Wife and Daughter for putting up with me, when long hours were spent at night staring at the data.

Table of Contents

ABSTRACT i
List of Figures v
List of Tables vii
List of Acronyms viii
Chapter 1: Introduction 1
1.1. Additive Manufacturing 2
1.2. Microstructures 4
1.3. Rapid Solidification 9
1.4. Ultrasound and Applications 10
1.5. Ultrasonic Transducer 14
1.5.1 Active Element: 14
1.5.2 Backing: 15
1.5.3 Wear plate: 15
1.6. Welding 16
1.6.1 Gas metal arc welding: 18
1.7. Summary 19
Chapter 2: Literature review 23
2.1. Ultrasonic application for porosity reduction and Grain structure refinement 23
2.2. Modelling efforts of Ultrasonic propagation 32
2.3. Rapid Solidification 34
2.4. Application of Ultrasonics in AM 36
2.5. Summary: 38
Chapter 3: Materials and Methodology 41
3.1. Experimental Setup 41
3.1.1. Low Cost Metal 3D Printer: 41
3.1.2. Ultrasonic Transducer: 45
3.1.3. Transducer and Workpiece Holder: 45
3.1.4. Transducer Driver 46
3.2. Methodology 49
3.2.1. Weld Bead Deposition 49
3.2.2. Sample Preparation 51

3.2.3. Optical Microscopy and Image processing: 53
3.2.4. Microhardness Testing: 55
3.3. Summary: 59
Chapter 4: Results and Analysis 61
4.1. Power Calculations: 61
4.2. Microstructure analysis: 64
4.3. Microhardness Analysis: 70
4.4. Summary: 79
Chapter 5: Conclusion and Future work 81
Appendix I: Experimental data 84
Appendix II: Instructions for Printer and Transducer control 85

List of Figures

Figure 1.1: Arduino Mega 2560 Microcontroller [1-6] 3
Figure 1.2: MIG welding using a metal 3D printer [1-8] 3
Figure 1.3: Processing techniques and their impact on the structure and properties [1-9] 4
Figure 1.4: Grain structures [1-11] 5
Figure 1.5: Grain boundaries [1-13] 6
Figure 1.6: Columnar grains in stainless steel [1-14] 7
Figure 1.7: Schematic diagram of low and high angle grain boundary [1-12] 8
Figure 1 8: Twist boundary [1-25] 8
Figure 1.9: Advantages and disadvantages of different processes [1-17] 10
Figure 1.10: Ultrasonic range [1-18] 11
Figure 1.11: Amplitude vs Time [1-18] 12
Figure 1.12: Transducer [1-18] 14
Figure 1.13: a) Immersion, b) Angle beam and c) Delay line transducers [1-22, 1-23, 1-24] 16
Figure 1.14: MIG welding [1-20] 18
Figure 2.1: Experimental setup [2-3] 25
Figure 2.2: Shaker [2-3] 26
Figure 2.3: SD vs Frequency [2-3] 26
Figure 2.4: Experimental setup [2-4] 27
Figure 2.5: Grain structure [2-4] 27
Figure 2.6: Micrographic results. a) SS b) SS-1350 c) SS-1387 [2-5] 29
Figure 2.7: Effect of melt purity on cavitation threshold [2-6] 30
Figure 2.8: Effect of ultrasonic treatment on primary silicon particles [2-6] 31
Figure 2.9: Mechanical properties of extrusions from ultrasonically treated hypereutectic Al-Si alloys and a 6063 alloy [2-6] 31
Figure 2.10: Schematic diagram of ultrasonic unit [2-8] 33
Figure 2.11: Rapid solidification techniques [2-9] 34
Figure 2.12: Scheaffler diagram of Steel samples [2-10] 35
Figure 2. 13: Microstructures of 316A and 316B laser welds [2-10] 36
Figure 2.14: Top and Side surface roughness [2-12] 38
Figure 3.1: Low-Cost Metal 3D Printer 42
Figure 3.2: Solidworks model of 3D metal printer [Source: Dr. Joshua Pearce, Michigan Tech University, 3-1] 43
Figure 3.3: Arduino Mega 2560 Motherboard 44
Figure 3.4: Arduino software interface 44
Figure 3.5: Ultrasonic transducer 45
Figure 3.6: Transducer and work piece holder 46
Figure 3.7: Transducer Driver Circuit 47
Figure 3.8: Driver Circuit (continued) 48

Figure 3.9: Oscilloscope image 49
Figure 3.10: Experimental setup 50
Figure 3.11: Weld bead selection 50
Figure 3.12: Zeiss Axiophot Optical Microscope 53
Figure 3.13: Image processing and analysis using imageJ. a) Image from optical microscope; b) Selection box; c) Background corrected; d) Binary image; e) Noise adjusted; f) Report generation; g) plots 55
Figure 3.14: NANOVEA M1 Hardness tester 56
Figure 3. 15: Measuring report of Berkovich indenter 56
Figure 3.16: Load- Displacement curve 58
Figure 4.1: NV S3 64
Figure 4.2: 20 LP S1 65
Figure 4.3: 38 HP S2 65
Figure 4.4: 56 LP S3 66
Figure 4.5: Porosity 38 HP S1 67
Figure 4.6: Grain count vs Treatment condition 68
Figure 4.7: Average area (μm^2) vs Treatment condition 68
Figure 4.9: Load curve NV 71
Figure 4.10: Load curve MF LP 72
Figure 4.11: Load curve HF LP 73
Figure 4.12: Hardness at HAZ (GPa) vs Treatment condition 74
Figure 4.13: Hardness at WB (GPa) vs Treatment condition 75
Figure 4.15: Young's modulus (GPa) vs Treatment condition at HAZ 77
Figure 4.16: Young's modulus vs Treatment condition at WB 77
Figure 4.17: Hardness vs Grain size and count 79

List of Tables

Table 3.1: Grinding 51
Table 3.2: Polishing 52
Table 4.1: Frequency and Power 62
Table 4.2: Design of Experiments 63
Table 4.3: Microstructure analysis results 67
Table 4.4: ANOVA results- Grain area 69
Table 4.5: ANOVA results- Grain count 70
Table 4.6: Microhardness test results 74
Table 4.7: ANOVA results- Hardness at HAZ 76
Table 4.8: ANOVA results- Hardness at WB 76
Table 4.9: ANOVA results- Young's modulus at HAZ 78
Table 4.10: ANOVA results- Young's modulus at WB 78

List of Acronyms

AM - Additive manufacturing
ASTM - American Society for Testing and Manufacturing
AW - Arc welding
CAD - Computer Aided Drafting
DFW - Diffusion welding
EWI - Edison Welding Institute
FRW - Friction Welding
FDM- Fused deposition modelling
GMAW - Gas Metal Arc Welding
HAZ - Heat affected zone
HF - High Frequency
HP - High Power
LF - Low Frequency
LP - Low Power
MF - Medium Frequency
MAG - Metal Active Gas welding
MIG - Metal Inert Gas welding
NV - No Vibration
OFW - Oxyfuel gas welding
RW - Resistance welding
SLM - Selective Laser Melting
SD - Standard deviation
SM - Subtractive Manufacturing
UAM - Ultrasonic additive manufacturing
USW - Ultrasonic welding
WB - Weld bead

Chapter 1: Introduction

This chapter gives an introduction to manufacturing and its evolution from the traditional practices to additive manufacturing (AM), significance of grain structures, rapid solidification ultrasonic vibrations, transducers and welding. In chapter 2, literature review and current findings on disruption of columnar grains are presented. Chapter 3 presents the methodology and experimental techniques used in this study. The obtained results, analysis and discussions are presented in chapter 4. Finally, chapter 5 summarizes the findings from this research and identifies future directions.

"Manufacturing", the word derived from the Latin words Manus (hand) and Factus (make) has its origins dating back to the Neolithic period with processes like carving, hand forming and firing of clay, grinding and polishing the stone and spinning, weaving and dyeing of cloth have been employed [1-1]. Manufacturing has undergone various revolutions from the Bronze Age to the Iron Age to Interchangeable parts, automated integration and is in the cusp of Additive Manufacturing (AM revolution. Some of the recent advancements can be attributed to the development of microelectronics, computerization, flexible manufacturing, microfabrication and nanotechnology, lean production and six sigma, globalization and environmental consciousness into traditional manufacturing [1-1].

There are several basic categories of manufacturing, i.e. solidification, forming, joining, subtraction and addition. This research focuses on rapid solidification observed in additive manufacturing (AM). AM, as the name suggests is a layer by layer deposition of the required material based on a 3D Computer Aided Drafting (CAD) model as opposed

to Subtractive Manufacturing (SM) which involves traditional manufacturing techniques like machining, drilling, grinding etc. to produce the desired part by removing material from a stock or bar. American Society for Testing and Manufacturing (ASTM) has classified AM into seven different categories namely, vat photopolymerization, material jetting, binder jetting, material extrusion, powder bed fusion, sheet lamination and direct energy deposition [1-2].

1.1. Additive Manufacturing

Material extrusion which is often called fused deposition modelling (FDM) is one of the commonly used AM process because of its relative ease to use and also, due to growing capabilities through open source development. Open source equipment is operated using free software and architecture developed by individuals/community of developers interested in one specific platform. It can be a 3D printer or a machine with a capability of producing self-replicating parts e.g. RepRap. Among several RepRaps, the most commonly employed structures are the delta and inverted delta which features expandable work envelope [1-4]. Some of the commercial AM machines can be obtained for $20,000 but often it can exceed over $1 million [1-4]. Due to the recent expiration of some of the patents related to FDM, a growing movement among developers and users has led to the creation of inexpensive AM machines [1-3].

Self-replicating rapid prototyping machine (RepRap) was among the early open source 3D printers [1-5]. The RepRap is a mechatronic device made of printed mechanical components for the frame, stepper motors to drive the extruder head and bed and a hot-end for melting polymer filaments [1-4]. These components are controlled by an open source microcontroller like Arduino® as shown in Figure 1.1.

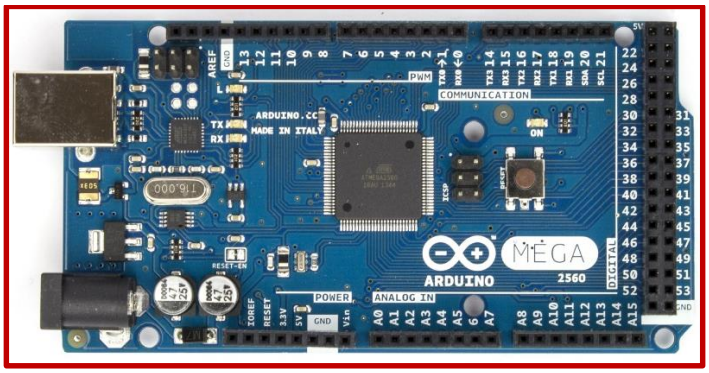

Figure 1.1: Arduino Mega 2560 Microcontroller [1-6]

Flexibility in open source RepRap has led to a rapid expansion in the development of low-cost polymer based AM. Until recently, there was a lack of similar efforts in metal AM and researchers were severely restricted to using expensive industrial grade printers. This motivated Dr. Joshua Pearce and his team to design an open source low cost metal 3D printer [7] which incorporates a low-cost commercial Metal Inert Gas (MIG) welder and is a derivative of the Rostock, a deltabot RepRap as shown in Figure 1.2.

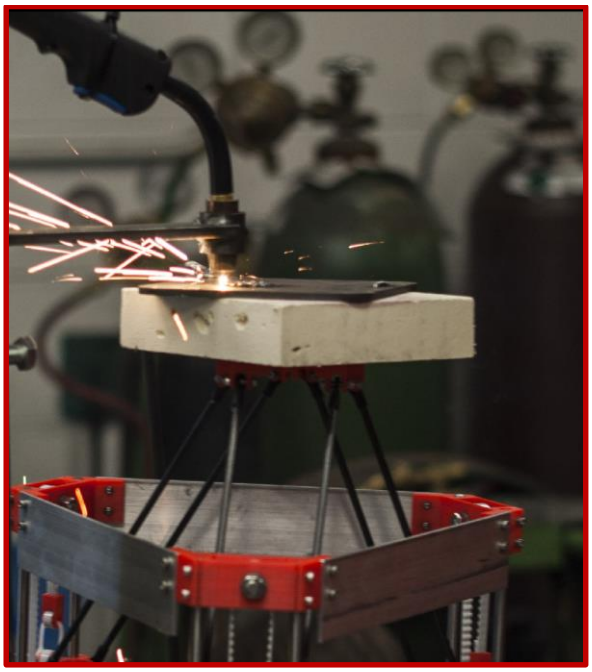

Figure 1.2: MIG welding using a metal 3D printer [1-8]

1.2. Microstructures

Over the years, many studies have been conducted to analyze and if possible refine the grain structures of the metals and alloys in order to have superior structural and mechanical properties. Some of the processing techniques and their impact on the structural and mechanical properties are shown in Figure 1.3.

Microstructural characterization includes:

1) Grains or crystals
2) Grain boundaries
3) Orientation of grains
4) Shape of grains
5) Phase compositions
6) Defects (i.e. voids, inclusions, etc.)

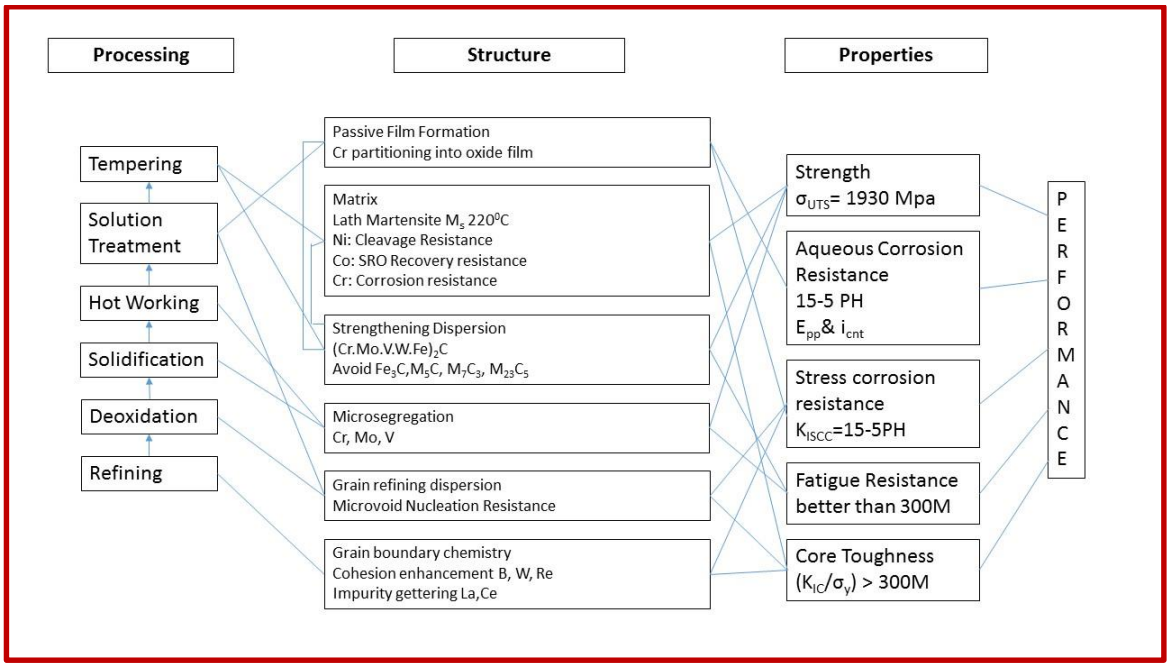

Figure 1.3: Processing techniques and their impact on the structure and properties [1-9]

Metal grains are comprised of individual, micro-nano sized randomly oriented crystals. When the molten metal starts to cool and solidify from the surface to the core of the molten pool, the grains tend to form in random directions at various locations known as nuclei. Depending on the cooling rate, the resulting grain sizes, grain counts and phase distributions will vary. Rapid cooling produces smaller grains while slower cooling rate results in larger sized grains. Nucleation (initial stage of formation of crystals) significantly influences the number and size of the grains i.e. if the nucleation rate is high; the number of grains developed is high with smaller grain size as shown in Figure 1.4 [1-10].

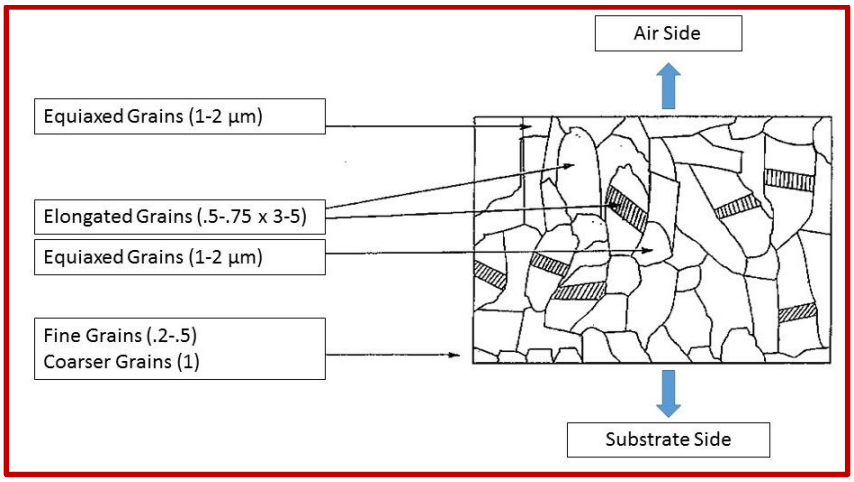

Figure 1.4: Grain structures [1-11]

The atomic mismatch where two grains with different crystallographic orientations results in an interfacial defect called the grain boundary is shown in Figure 1.5 [1-12].

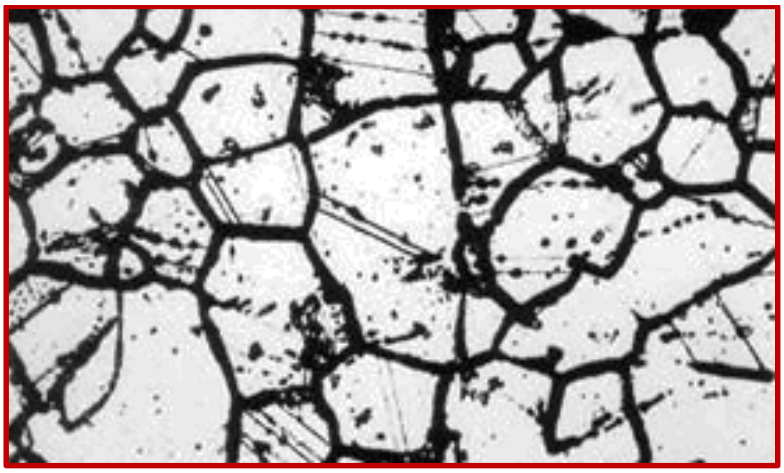

Figure 1.5: Grain boundaries [1-13]

The grain boundaries have an important influence on the mechanical properties of metals like strength, ductility as it interferes with the dislocation movement and also influences strain hardening. The effect of grain boundaries varies with temperature, deformation rate and impurities present along the grain boundaries [1-3]. Columnar grains are long, thin, coarse grains created when molten metal solidifies rather slowly in the presence of a steep temperature gradient. Relatively few nuclei are available when columnar grains are produced as shown in Figure 1.6.

The smaller the grain size, the greater the number of the grain boundaries. Presence of more grain boundaries leads to a higher resistance to slip (during plastic loading conditions). In addition equiaxed grains leads to a more uniform mechanical properties within the part (isotropy).

The Hall-Petch effect correlates the trend of increasing strength and toughness with decreasing grain size [1-12]. Creep rates (Coble creep) increase with increasing grain boundary (per unit volume), hence decreasing grain size. Therefore grain size has the opposite effect at high temperatures where finer grain size weakens the material. Hence,

finer grain size is preferred in low temperature applications and single crystals (also known as whiskers) are ideal for high temperature applications.

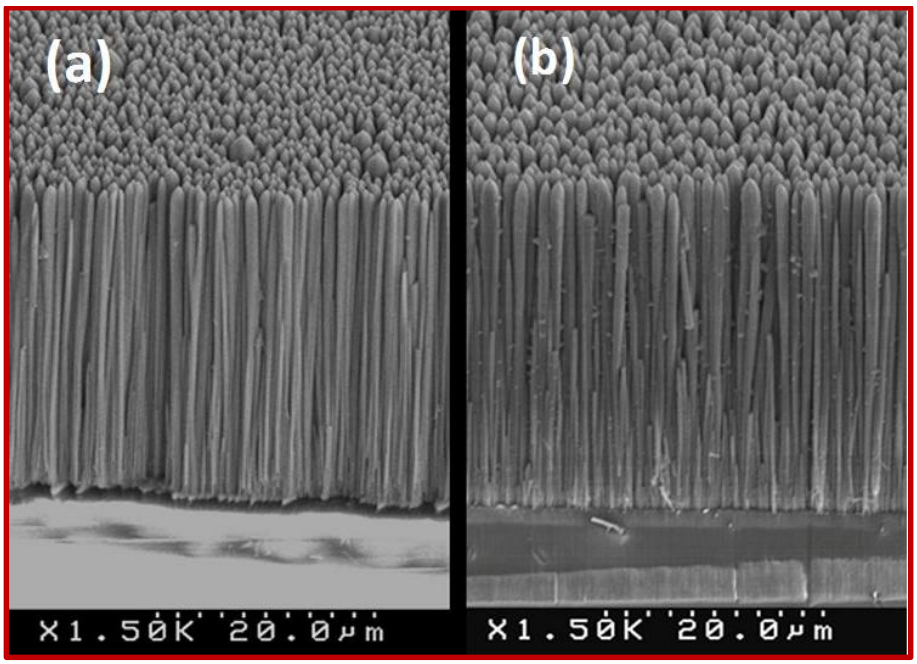

Figure 1.6: Columnar grains in stainless steel [1-14]

As shown in Figure 1.7, the crystallographic misalignment between adjacent grains is noted based on the angle of misalignment at the grain boundaries. When the orientation mismatch is in the order of a few degrees then it is called small angle grain boundary.

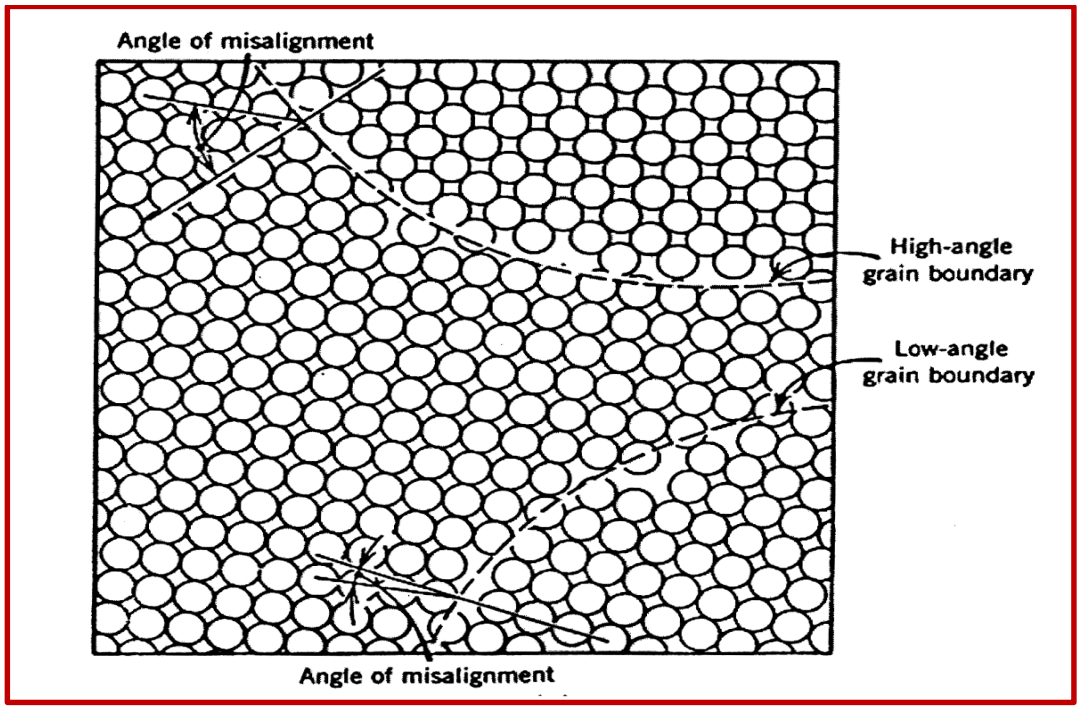

Figure 1.7: Schematic diagram of low and high angle grain boundary [1-12]

Twist boundary as shown in Figure 1.8, is formed when a small angle grain boundary with a tilt has an angle of misorientation θ parallel to its boundary. An array of screw dislocations gives the perfect illustration of twist boundary. The bond angles are longer at grain boundaries, as there is an accumulation of grain boundary energy. The magnitude of grain boundary energy is a function of the degree of misorientation.

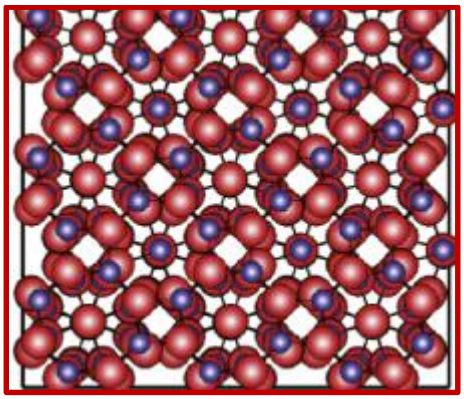

Figure 1 8: Twist boundary [1-25]

1.3. Rapid Solidification

Rapid solidification is a processing technique by which unusual properties and microstructures can be obtained, which by conventional processing techniques is not possible [1-15].

Some of the manufacturing processes in which rapid solidification is observed are:

- Vacuum induction melting
- Squeeze casting
- Splat quenching
- Melt spinning
- Planer flow casting
- Laser or electron beam solidification

Paul Duwez and others created a new frontier for the processing of materials in rapid solidification over a quarter of a century ago [1-16]. Though they were not the first to investigate rapid solidification rate techniques (sometimes called as rapid quenching), it was the efforts of Duwez that started the revolution in rapid solidification technology. His initial experiments involved melting a small amount of metal at the bottom of a tube and ejecting the molten metal onto a copper plate using sudden gas pressurization which results in a "splat" of frozen metal with a solidification rate on the order of 10^6 K/s [1-16]. Traditionally, the cooling rate of 10^4 K/s or greater is considered as rapid solidification [1-16]. However, there are other studies that have identified single-pass welding of smaller melt pool at a cooling rate of 10 K/s as rapid solidification [1-26]

Though rapid solidification has several advantages for a variety of applications, it has some limitations as shown in Figure 1.9.

Process	Advantages	Limitations
Spray Pyrolysis	Effective preparation of ultra fine, spherical and homogeneous powders in multicomponent systems,reproductive size and quality.	High cost associated with producing large quantities uniform, nanosized partic
Liquid Infiltration	Short contact times between matrix and reinforcements; moulding into different and near net shapes of different stiffness and enhanced wear resistance; rapid solidification; both lab scale and industrial scale production.	Use of high temperature; segregation of reinforcements; formation undesired products during processing.
Rapid Solidification Process (RSP)	Simple; Effective	Only metal-metal nanocomposites; induced agglomeration and non-homogeneous distribution fine particles.
RSP with ultrasonics	Good distribution without agglomeration, even with fine particles.	
High Energy Ball Milling CVD/PVD	Homogeneous mixing and uniform distribution. Capability to produce highly dense and pure materials; uniform thick films; adhesion at high deposition rates; good reproducibility.	Optimization of many parameters; cost; relative complexity.
Chemical Processes (Sol-Gel, Colloidal)	Simple; low processing temperature; versatile; high chemical homogeneity; rigorous stoichiometry control; high purity products.	Weak bonding. low wear-resistance. high permeabi and difficult control of porosity.

Figure 1.9: Advantages and disadvantages of different processes [1-17]

1.4. Ultrasound and Applications

Ultrasounds are acoustic waves generated beyond range of human hearing i.e. above 20 Hz - 20 kHz. In principle, ultrasound behaves similar to audible sound, but it has a much shorter wavelength and can be used to identify defects inside materials (e.g. nondestructive testing). The categories of acoustic spectrum as shown in Figure 1.10 are: 1) subsonic range, 2) audible range and 3) ultrasonic range. The ultrasonic range is then

further broken into 3 sub sections; 1) low frequency/airborne/high frequency, 2) conventional/industrial, 3) high frequency/ acoustic microscopy.

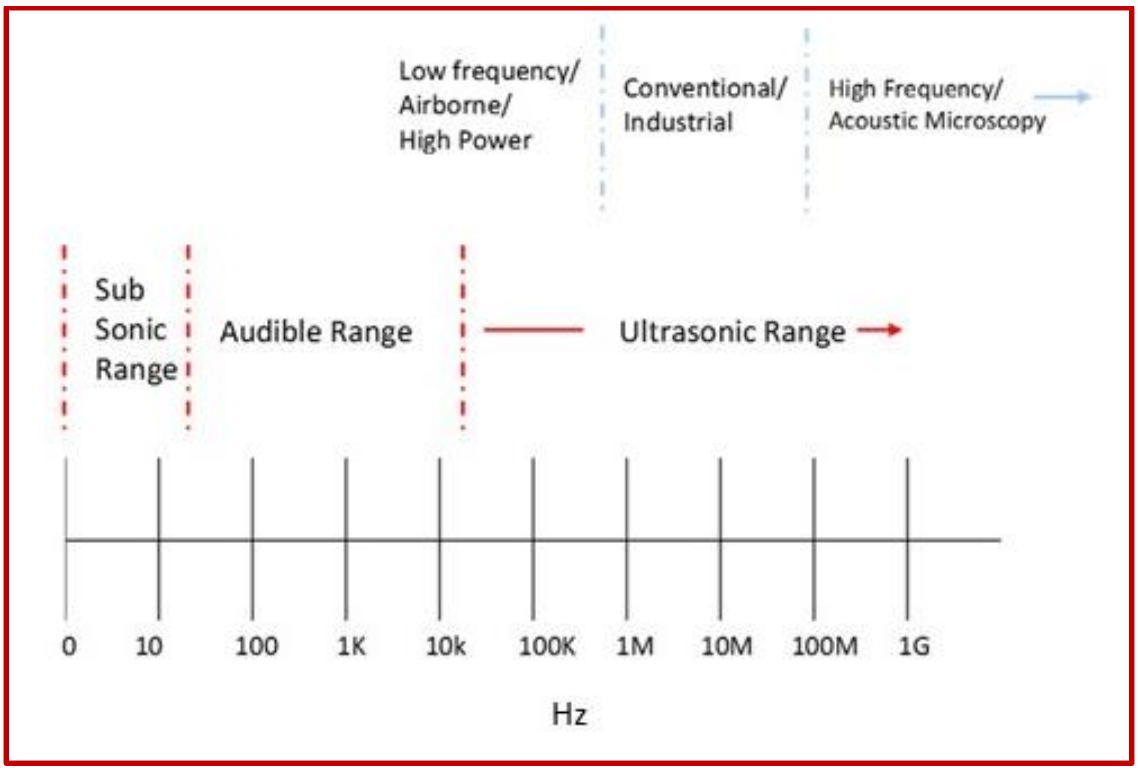

Figure 1.10: Ultrasonic range [1-18]

Transmission of ultrasounic waves requires an elastic medium which can be gas or liquid or solid. Glycerin and water are the two most commonly used medium. The basic parameters of a Continuous Wave (CW) are wavelength (l) and the period (T) of a complete cycle as shown in Figure 1.11.

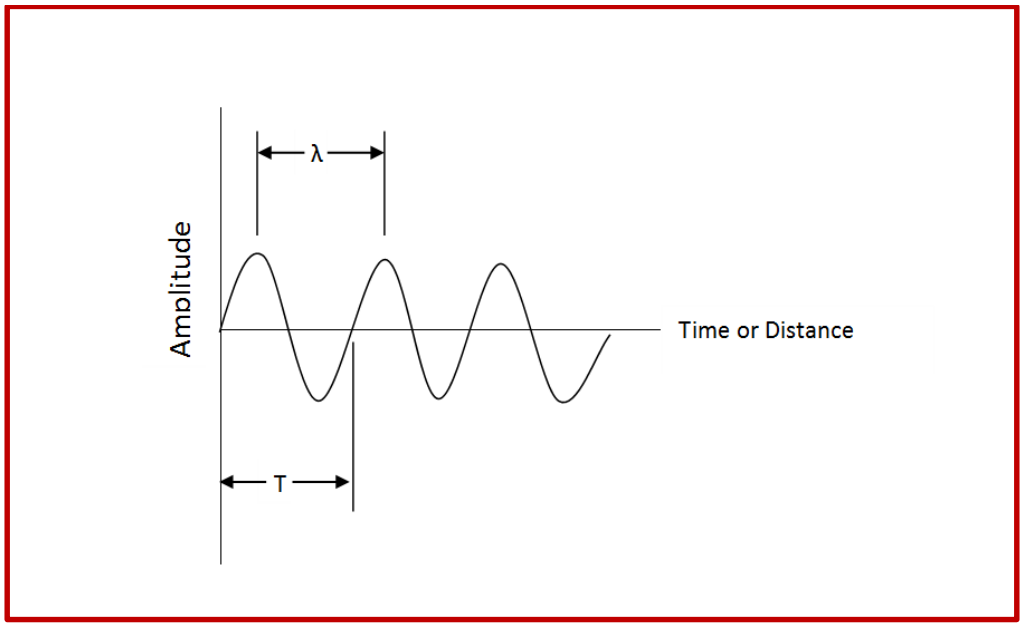

Figure 1.11: Amplitude vs Time [1-18]

The number of cycles completed in one second is called frequency (f) and is measured in Hertz (Hz), some examples follow;

- 1 cycle/second= 1Hz
- 1000 cycles/second= 1kHz
- 1,000,000 cycles/second= 1MHz

The time required to complete a full cycle is the period (T), measured in seconds. The relation between frequency and period in a continuous wave is given as:

$$f = 1/T \tag{1.1}$$

Common methods of ultrasonic examination utilize either longitudinal waves or shear waves. Other forms of sound propagation include surface waves and Lamb waves [1-18]. The longitudinal wave is a compressional wave in which the particle motion is in the same direction as the propagation of the wave. The shear wave is a wave motion in which the particle motion is perpendicular to the direction of the propagation. Surface

(Rayleigh) waves have an elliptical particle motion and travel across the surface of a material. Their velocity is approximately 90% of the shear wave velocity of the material with the depth of penetration approximately equal to one wavelength. Plate (Lamb) waves have complex vibration as they are elastic waves whose particle motion lies in the plane containing the wave propagation and perpendicular to the plate and occurring in materials where thickness is less than the wavelength of the ultrasound [1-18].

Sensitivity is the ability of an ultrasonic system to detect reflectors (or defects) at a given depth in a test material. Axial resolution is the ability of an ultrasonic system to produce simultaneous and distinct indications from reflectors located at nearly the same position with respect to the sound beam. Near surface resolution is the ability of the ultrasonic system to detect reflectors located close to the surface of the test piece [1-18].

The ultrasound can be categorized as power ultrasonics if the frequency ranges from 10 kHz to 500 kHz. Power ultrasonics can be applied to permanently change the physical, chemical or biological properties of the object [1-19].

Some of the applications of power ultrasonics are:

- Welding, metal forming and machining; e.g. ultrasonic spot welding, Plunge ultrasonic welding, wire and tube drawing, surface grinding etc.
- Engineering and medical applications; e.g. ultrasonic motors, ultrasound synthesis of metallic nanoparticles, Ultrasonic cleaning and washing, Ultrasonic surgical devices etc.
- Food technology and pharmaceuticals, e.g. ultrasonic mixing, homogenization and emulsification, Ultrasonic atomization for encapsulation for drug delivery etc.

- Environmental, mining, biofuel production e.g. ultrasonic water treatment etc.

1.5. Ultrasonic Transducer

A transducer is a device that converts one form of energy to another. An ultrasonic transducer converts electrical energy to mechanical energy, in the form of sound and vice versa. The main components are active element, backing, and wear plate as shown in Figure 1.12.

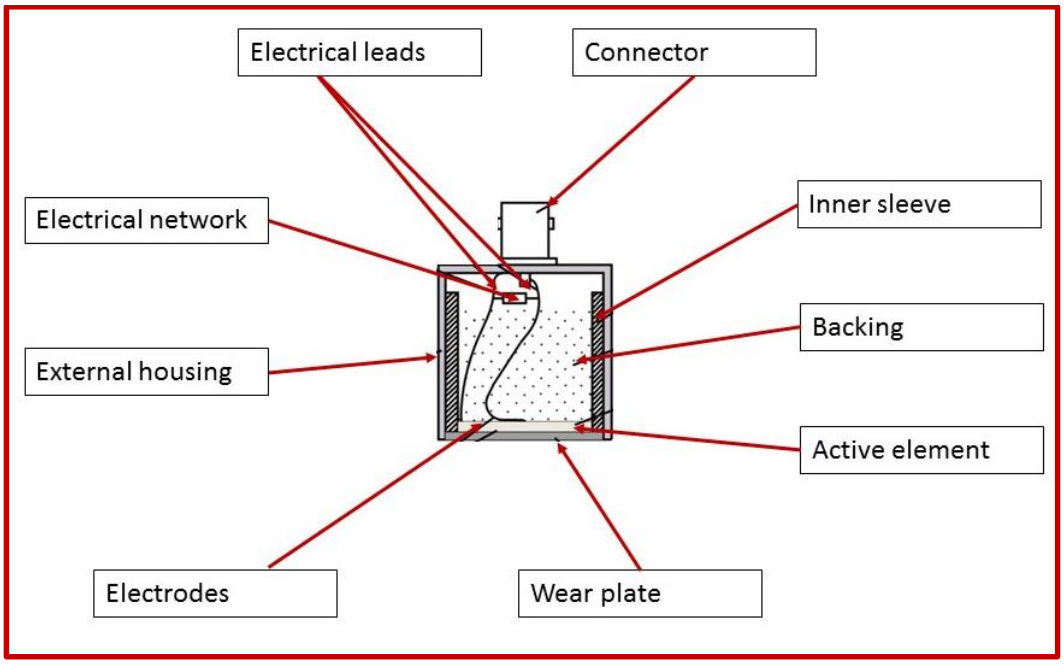

Figure 1.12: Transducer [1-18]

1.5.1 Active Element:

The active element made of piezo or ferroelectric material converts electrical energy such as a pulse from a flaw detector into ultrasonic energy. The most commonly used materials are polarized ceramics which can be cut into various geometries to produce different wave modes. New materials such as piezo polymers and composites are also

being employed for applications where they provide benefits with efficient ultrasonic energy generation to transducer and system performance. [1-18]

1.5.2 Backing:

The backing is usually a highly attenuative, high density material that is used to control the vibration of the transducer by absorbing the energy radiating from the back face of the active element. When the acoustic impedance of the backing matches the acoustic impedance of the active element, the resulting transducer will be heavily damped with good range resolution but lower signal amplitude. If there is a mismatch in acoustic impedance between the element and the backing, more sound energy will be reflected into the test material. In this case, the transducer will have lower resolution due to longer waveform duration, but higher signal amplitude and lower sensitivity [1-18].

1.5.3 Wear plate:

The basic purpose of the transducer wear plate is to protect the transducer element from the operating environment. In the case of contact transducers, the wear plate is made of a durable and corrosion resistant material in order to withstand the wear caused by use on ferrous metals due to lower impedance.

There are three different types of ultrasonic transducers 1) immersion, 2) angle beam, and 3) delay line transducers as shown in Figure 1.13. The wear plate for the transducers also serves as an acoustic transformer between the high acoustic impedance of active element and water, wedge or delay line. This is accomplished by selecting a matching layer that is $1/4^{th}$ wavelength thick ($\lambda/4$) and of the desired acoustic impedance (the active element is nominally $1/2^{th}$ wavelength). The choice of the wear surface thickness is based on the

principle of superposition, which defines that the net response given at a place and time by two or more stimuli which is the sum of responses of each stimulus individually, which allows waves generated by active element to be in phase with wave reverberating in the matching layer. When the signals are in-phase, their amplitudes are additive, thus a resulting in a higher greater amplitude wave.

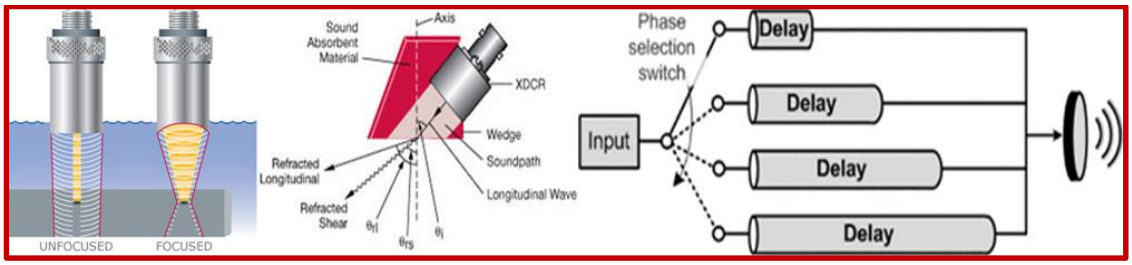

Figure 1.13: a) Immersion, b) Angle beam and c) Delay line transducers [1-22, 1-23, 1-24]

In such cases, when the signals are in-phase their amplitudes are additive resulting in a higher amplitude. If a transducer is not properly designed or tightly controlled or constructed with improper materials are it would result in generation of waves that are not in-phase, causing disruptions in the wave front [1-18].

1.6. Welding

Welding is a joining process in which two materials are bonded together at atomic level to achieve a joint which are permanent. Welding process is achieved by heat, pressure and different combinations of both. Although it started around 1000 B.C, Egyptians and other eastern Mediterranean areas developed the technique of forge welding, it was not until 1801 that carbon arc welding was discovered by Sir Humphrey Davy and later refined by Nikolai Benardos in 1885. Charles Coffin developed arc welding process using metal electrode in 1892.

The major advantages of welding are:

1. Creation of permanent joints
2. Ability to use filler material
3. Often economical to join components
4. Portability

The limitations of welding are:

1. Relatively higher labor cost
2. Relatively higher energy usage
3. Creation of permanent joints limiting ability to unjoin
4. Columnar grain structures

There are two major categories of welding namely fusion welding and solid state welding. Fusion welding process utilizes heat to melt the base metals. The different types of fusion welding processes are:

1) Arc welding (AW)
2) Resistance welding (RW)
3) Oxyfuel gas welding (OFW)
4) Electron beam welding
5) Laser beam welding

Solid state welding uses either pressure alone or a combination of both heat and pressure to achieve the required joining. The different types of solid state welding processes are:

1) Diffusion welding (DFW)
2) Friction Welding (FRW)
3) Ultrasonic welding (USW)

1.6.1 Gas metal arc welding:

The main components of Gas Metal Arc Welding (GMAW) or Metal Inert Gas welding (MIG) or Metal Active Gas welding (MAG) as shown in Figure 1.14 are:

- Welding gun
- Solid wire electrode

The process parameters of GMAW include:

- Shielding gas e.g. Argon
- Electrode size e.g. 0.023”
- Voltage and current e.g. 110-240V
- Feed rate e.g. 45 ipm
- Travel speed e.g. 5.52 ipm

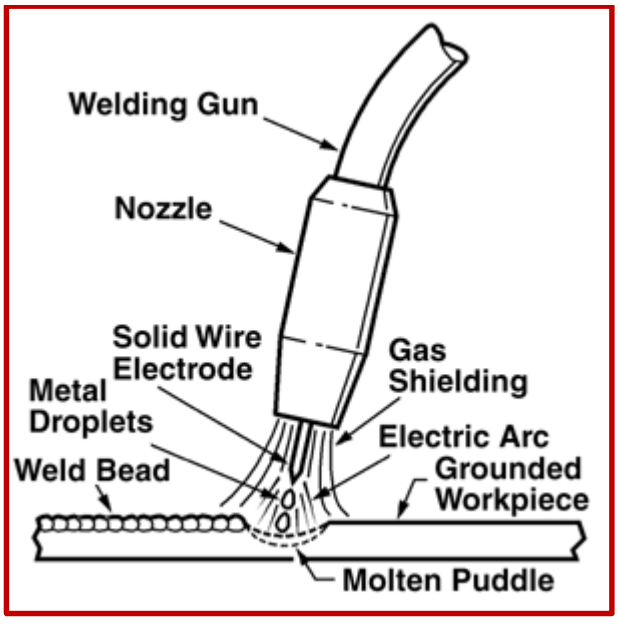

Figure 1.14: MIG welding [1-20]

The principle of MIG welding is arc burning between the solid wire electrode that is constantly fed from a spool with pre-determined feed rate and the work piece with a

constant voltage, direct current. A protective gas shield (Ar and CO_2) is fed through the welding gun to avoid both the electrode material and work piece reacting with atmosphere [21].

1.7. Summary

In summary, this chapter defined the basic concepts of additive manufacturing and its evolution from being patent bound to open source, creating a flexibility for researchers to create low cost equipment as per the requirements. The concepts of rapid solidification and its applications in various industries have been explained. Also microstructures and impact of rapid solidification on the microstructures has been introduced. Finally the various components of a power ultrasonic transducer and its applications have been introduced.

References:

1-1 Mikell P. Groover, Fundamentals of modern manufacturing materials, processes and systems, Fourth ed., New Jersey, John Wiley & Sons, Inc., 2010

1-2 Russ, Harris, “About additive manufacturing”, URL: http://www.lboro.ac.uk/research/amrg/about/the7categoriesofadditivemanufacturing/ July 14th 2015 accessed

1-3 Serope Kalpakjian and Steven R. Schmid, Manufacturing engineering and technology, Seventh ed., New jersey, Pearson education Inc., 2013

1-4 Pearce, J. M., Open-Source Lab. New York: Elsevier, 2014

1-5 RepRap, "RepRap", RepRap wiki , URL: http://www.reprap.org/, July 9th 2015 accessed.

1-6 Arduino, “Arduino Mega 2560”, ArduinoBoardMega2560, URL: https://www.arduino.cc/en/Main/ArduinoBoardMega2560, July 9th 2015 accessed

1-7 Open-source Metal 3-D printer, “Open-source Metal 3-D printer”, Appropedia: the sustainability wiki, URL: http://www.appropedia.org/Open-source_metal_3-D_printer, 21st September 2014 accessed

1-8 A low cost open source metal 3d printer by Gerald C. Anzalone, Chenlong Zhang, Bas Wijnen, Paul G. Sanders, and Joshua M. Pearce, 10.1109/ACCESS.2013.2293018

1-9 AZoM.com staff writers, “Application of Integrated Computational Material Engineering to Design and Develop New Alloys”, Application of Integrated Computational Material Engineering to Design and Develop New Alloys, URL: http://www.azom.com/article.aspx?ArticleID=10463 24th July 2014 accessed

1-10 Serope Kalpakjian and Steven R. Schmid, Manufacturing processes for engineering materials, Fifth ed., New jersey, Pearson education Inc., 2008

1-11 Emeraldinsight, URL: http://www.emeraldinsight.com/content_images/fig/2170260401002.png July 18th 2014 accessed

1-12 William D. Callister, J., Materials Science And Engineering An Introduction. Fourth ed. New York, Toronto: John Wiley & Sons, Inc., 1997

1-13 Weld reality, URL: http://www.weldreality.com/grain-boundry.gif July 18th 2014 accessed

1-14 Intechopen, URL: http://www.intechopen.com/source/html/41430/media/image14_w.jpg July 15th 2015 accessed

1-15 Rapid solidification processing of high T_c super conductors: Microstructural features and phase relationships by J. M_cKittrick, M.E.M_cHenry, C. Heremans, P. Standley, T.R.S Prasanna, G. Kalonji, R.C. O'Handley and M. Foldaeki, Physica C 153-155(1988) 369-370

1-16 The role of rapid solidification processing in fabrication of fiber reinforced metal matrix composites by Ivan E. Locci and Ronald D. Noebe, NASA-TM-l0l450, 1989

1-17 Materials research, URL: http://www.scielo.br/scielo.php?script=sci_arttext&pid=S1516-14392009000100002 July 24th 2014 accessed

1-18 Olympus, "Ultrasonic transducers technical notes", URL: https://www.olympus-ims.com/data/File/panametrics/UT-technotes.en.pdf , July 24th 2015 accessed

1-19 Juan A. Gallego- Juarez and Karl F. Graff, Power ultrasonics applications of high intensity ultrasound, Elsevier, 2014

1-20 Image.thefabricator.com, URL: http://image.thefabricator.com/a/articles/photos/301/fig1.gif July 18th 2014 accessed

1-21 Gas metal arc welding, URL: http://www.ukessays.com/essays/education/gas-metal-arc-welding.php July 18th 2014 accessed

1-22 Static2.olympus-ims.com, URL: http://static2.olympus-ims.com/data/Image/harisonic_transducers/Unfocused_Focused.jpg?rev=CC80 July 26th 2015 accessed

1-23 Static3.olympus-ims.com, URL: http://static3.olympus-ims.com/data/Image/fd-tutorial/5.2_angle_beam12.jpg?rev=B7EF July 26th 2015 accessed

1-24 Mdpi.com, URL: http://www.mdpi.com/sensors/sensors-11-00539/article_deploy/html/images/sensors-11-00539f4-1024.png July 26 th 2015 accessed

1-25 Iopscience, URL: http://cdn.iopscience.com/images/0953-8984/25/35/355001/Full/cm472973f1_online.jpg July 20 th 2015 accessed

1-26 S.A. David, S.S. Babu, and J.M. Vitek, "Welding: Solidification and Microstructure", URL: http://www.tms.org/pubs/journals/JOM/0306/David-0306.html , July 24th 2015 accessed

Chapter 2: Literature review

In this chapter, a review of literature focused on ultrasonic application for porosity reduction and grain structure refinement, modeling efforts of ultrasonic propagation, rapid solidification and applications of ultrasonics in Additive Manufacturing (AM) is presented. As mentioned in chapter 1, ultrasonic transducers can be basically classified into contact type and non-contact type. Non-contact type transducers are mainly applied for navigation (e.g. SONAR) and the contact type transducer have broader applications in engineering, medical, material science and also, in the food processing industry. Since this experiment is related to manufacturing and processing of materials, ultrasonic transducers which are applied for microstructure refinement and porosity control are emphasized.

2.1. Ultrasonic application for porosity reduction and Grain structure refinement

John. A. Slotwinski and his team worked on porosity measurements and analysis for metal Additive Manufacturing (AM) process control [2-1]. It was identified that material porosity in parts is undesirable for aerospace parts, since it could lead to premature failure and sometimes be desirable in biomedical implants, as surface-breaking pores allows for better integration with biological tissue. Variability in the porosity during AM process can also be attributed to the variability in feedstock, process parameters and conditions. They worked on developing an ultrasonic sensor for monitoring changes in the porosity in metal parts during fabrication on a metal powder bed fusion system. The measurements of the porosity of these samples using Archimedes and X-Ray Computed Tomography (XRCT), and a correlation of ultrasonic measurements with the degree of

porosity were presented using a 5MHz commercial contact type piezoelectric ultrasonic transducer.

They concluded that the porosity level in these parts was controlled by varying the build parameters in the Direct Metal Laser Sintering System (DMLS) process for each of the disks. Comparisons of the measured composite disk porosity, which was determined using Archimedes and mass of the cylinders, were in agreement. However, the large error bars on the disks' composite porosities determined from the individual cylinder measurements is an indication of the local differences in disk porosity that were inherent in the cylinders cut out of those disks. The XRCT also showed the presence of cracks, which sometimes cross the laser scan lines from the DMLS process. These cracks were routinely present for the samples that had a large amount of porosity. These samples also had pores that connected across many measured layers.

Sandia National Laboratories has developed Laser Engineered Net Shaping (LENS®), a new technology to fabricate 3D metallic components directly from CAD solid models. Metal parts are fabricated directly from the Computer Aided Design (CAD) solid models using a metal powder injected into a molten pool created by a high-powered laser beam on an NC motion controlled substrate to fabricate the desired cross-sectional geometry. Consecutive layers are deposited until the final part geometry is produced. Parts have been fabricated in stainless steel alloys, nickel-based alloys, tool steel alloys, titanium alloys, and other specialty materials; as well as composite and functionally graded material deposition using LENS. Sometimes, ultrasonic vibration to base plate is applied in order to improve the quality of the part produced because of the tighter packing of the

powder during deposition. This process improved the mechanical properties of the resultant products and reduced the time required for part processing.

Ehsan Foroozmehr and his team worked on improving the quality in the Laser Powder Deposition (LPD) by using in-process vibration by integrating a vibration system into a laser-cladding system. A 1-kW Nd:YAG laser system along with a powder delivery as shown in Figure 2.1 in a 5-axis CNC vertical machining center with protective argon gas flow was used in the vibrator setup was placed on the x-y table which holds the substrate. An electromagnetic shaker is tightly connected to the aluminum plate as shown in Figure 2.2. A signal generator is connected to a 400W amplifier [2-3].

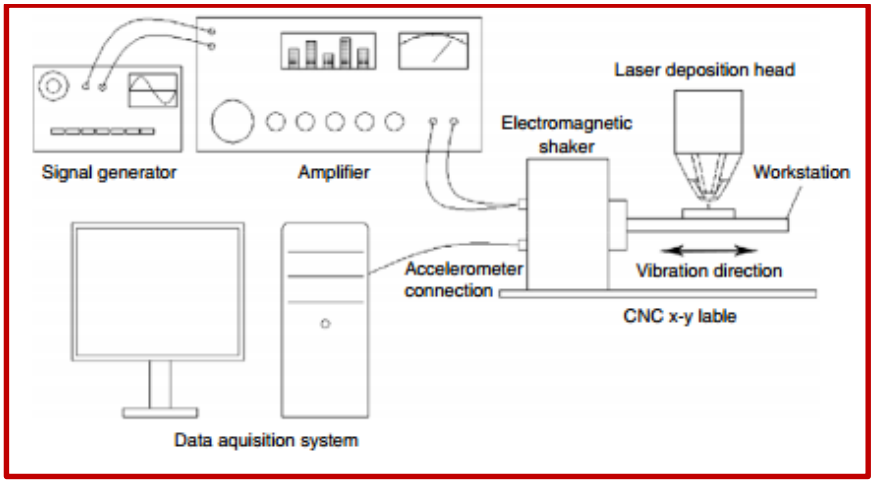

Figure 2.1: Experimental setup [2-3]

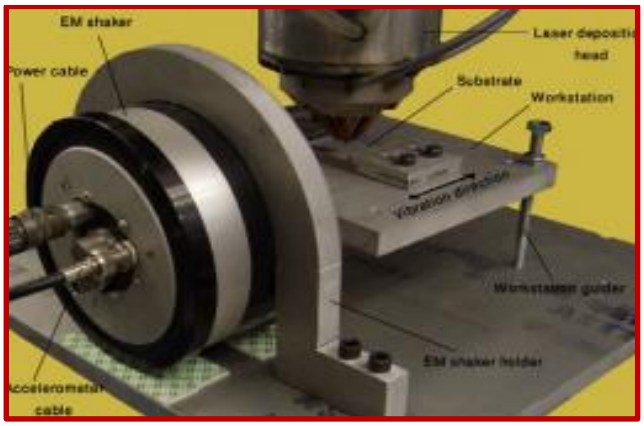

Figure 2.2: Shaker [2-3]

The experiment resulted in the mitigation of defects at the intersection of beads and reduction in spherical gas pockets which result in porosity.

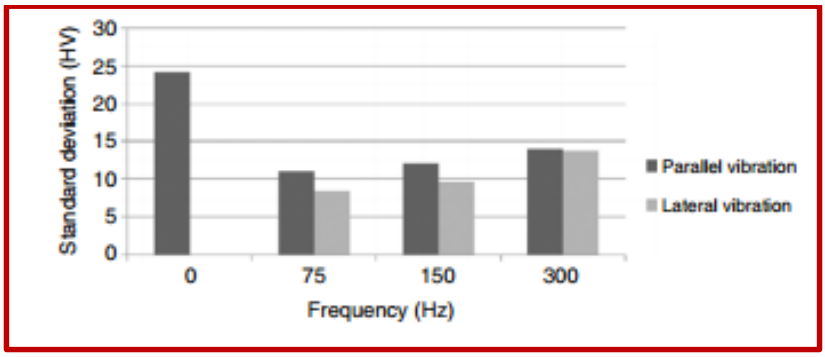

Figure 2.3: SD vs Frequency [2-3]

The results in Figure 2.3 showed that the lateral vibration was more effective than parallel vibration and a dendritic zone under vibratory conditions consists of smaller grains and increased the hardness when compared to no vibration [2-3].

Longbiao He and others studied [2-4] ultrasonic generation by modulated welding arc and analyzed its effects on grain structure refinement as shown in Figure 2.4. Their work showed that the acoustic response of pulsed arc indicated that the arc could be considered as an ultrasonic transducer, with the experimental setup as shown in Figure 2.5.

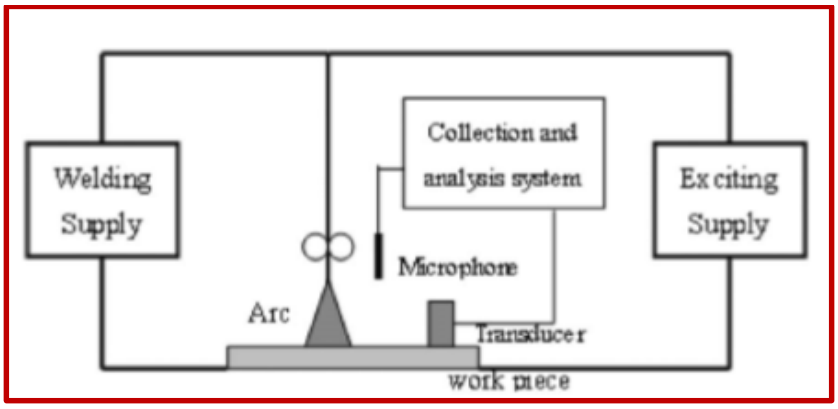

Figure 2.4: Experimental setup [2-4]

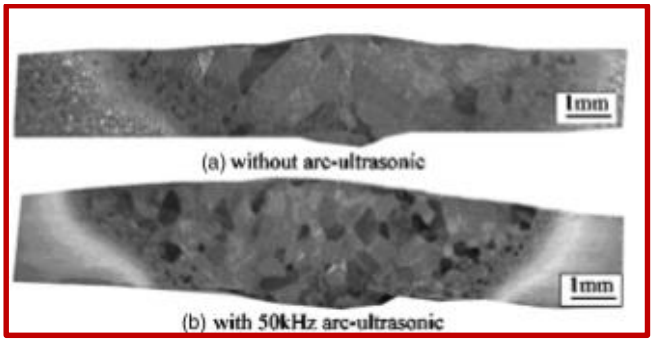

Figure 2.5: Grain structure [2-4]

They observed that with exciting welding arc, the welding structure could be refined and improve performance of joints by reducing porosity and inclusion to welding joint. Their method stated that the ultrasonic emission can take place wherever the arc is present and can be used in arc welding, plasma welding, thermal spraying process, etc., to improve the performance of material processing [2-4].

Jafar Saniie and Nihat M. Bilgutay [2-5] quantified the grain size evaluation using ultrasonic backscattered grain signals, which applies a similar concepts of SONAR which transmits and receives ultrasonic signals to determine the position and distance by investigating a heuristic model to relate the statistical characteristics of the measured signal to the mean ultrasonic wavelet and attenuation coefficient in different regions of

the sample. Heat treated stainless steel (SS) samples of various grain sizes were used. Temporal averaging, correlation and probability distribution functions of the data set techniques were used to examine the losses in the backscattered signal losses. Frequency dependent attenuation, homomorphic processing was performed to estimate the mean ultrasonic wavelet as it propagates through the sample.

They considered three different SS samples 1) without heat treatment, 2) heat treated SS at 1350 ^{0}C and 3) heat treated SS at 1387 ^{0}C. The average grain diameters of the three samples were calculated by approximating it to be twice the average grain boundary spacing. The micrographs they obtained are as shown in Figure 2.6, which shows the average grain size and boundary spacing.

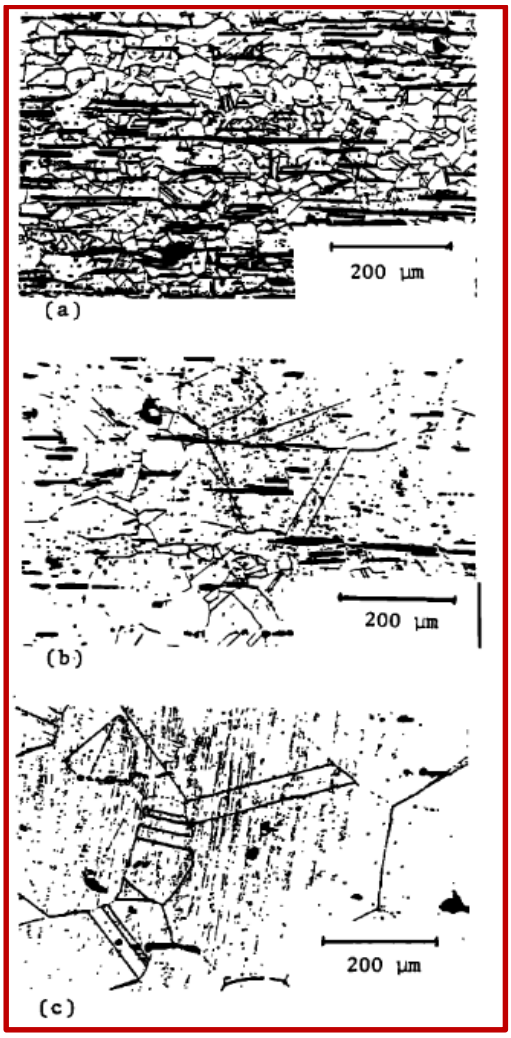

Figure 2.6: Micrographic results. a) SS b) SS-1350 c) SS-1387 [2-5]

A high sensitive Gamma type transducer with a nominal frequency of 6-MHz and a 3-dB bandwidth of approximately 1.5 MHz was used. The transducer is excited by generating pulses of width on the order of a few nanoseconds. To eliminate ambiguity of the receiving signals received for the Region of Interest (ROI), the pulse reception rate was 200 pulses and a range gate was used to filter only the required signals. Their results indicated that various signal processing techniques could be utilized in ultrasonic grain size evaluation. All techniques are concerned with removing the randomness in the

backscattered signal and extracting parameters related to the frequency-dependent attenuation coefficient and, consequently, to the grain size [2-5].

G.I. Eskin and D.G. Eskin worked on ultrasonic treatment of the natural and synthesized aluminum based composite materials. In their study, they found that as the contamination of the samples increases, the cavitation threshold decreases leading to less acoustic energy required for cavitation onset. This phenomenon was observed at a constant hydrogen content in aluminum of 0.2 cm^3 /100 g and 1) 0.03, 2) 0.008, 3) 0.005 and 4) 0.004% Al_2O_3 was plotted and is as shown in Figure 2.7 [2-6].

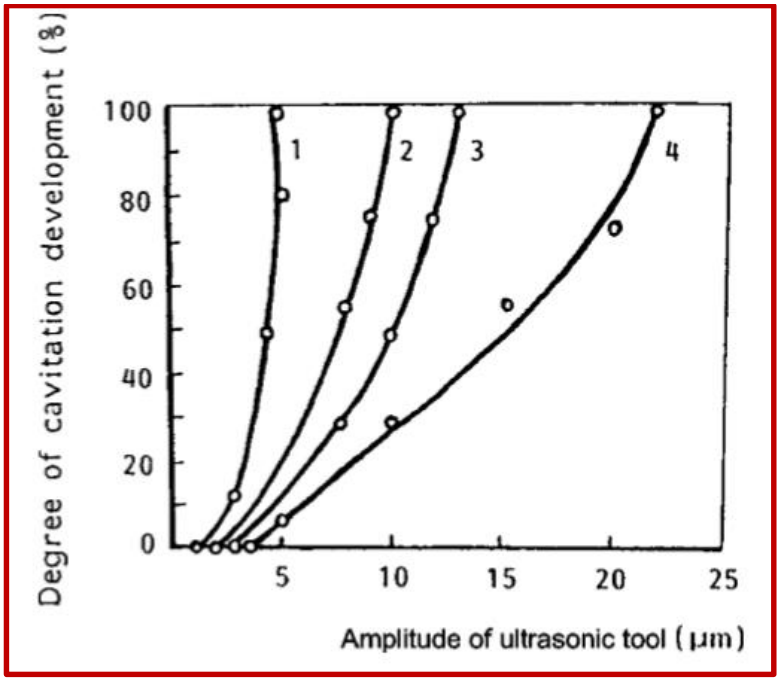

Figure 2.7: Effect of melt purity on cavitation threshold [2-6]

They observed powerful refinement of primary silicon particles when ultrasonic treatment applied upon solidification of hypereutectic Al-Si alloys, for 114-mm DC cast ingots at the ultrasonic tool amplitude 15μm and is as showed in Figure 2.8 [2-6].

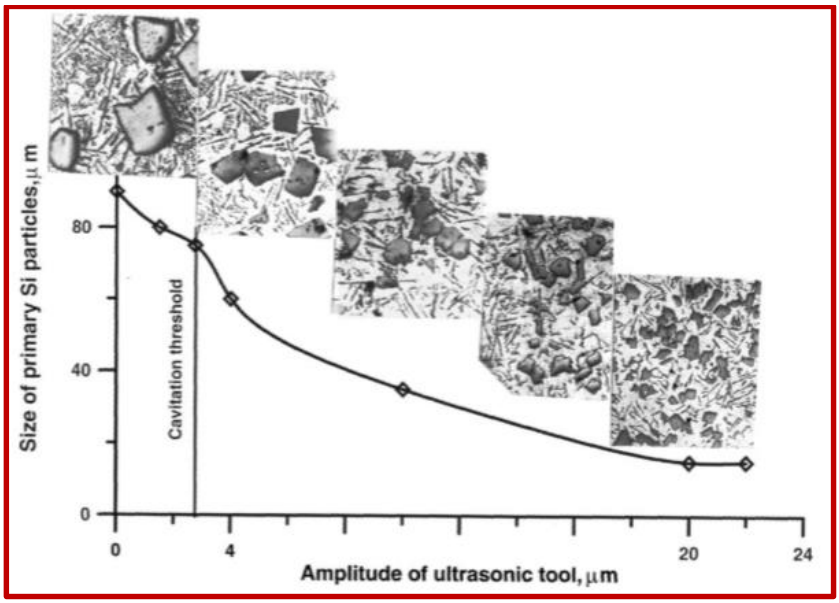

Figure 2.8: Effect of ultrasonic treatment on primary silicon particles [2-6]

The ultrasonic treatment also had significant impact on the mechanical properties like 25% lower linear coefficient of thermal expansion, 15% higher Young's modulus and improved wear and corrosion resistance along with excellent weldability and they are as shown in Figure 2.9 [2-6].

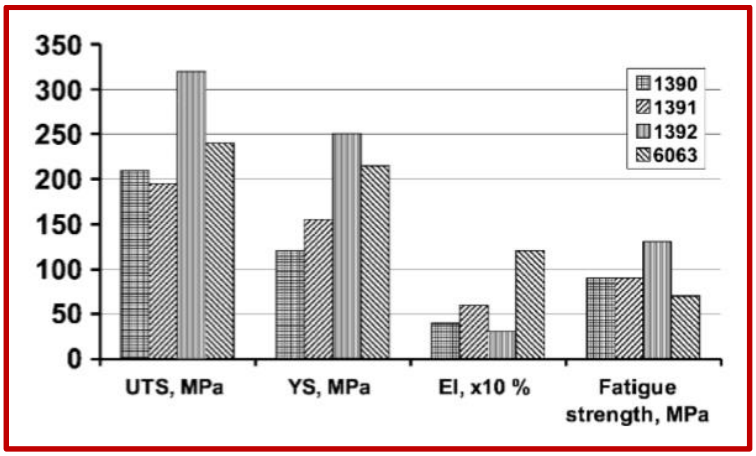

Figure 2.9: Mechanical properties of extrusions from ultrasonically treated hypereutectic Al-Si alloys and a 6063 alloy [2-6]

2.2. Modelling efforts of Ultrasonic propagation

A. Gandin and M. Rappaz worked on developing a 3D cellular automaton (CA) algorithm for predicting the dendritic grain growth. The CA growth algorithms were validated by comparing the predicted grain shapes with those deduced from analytical models. The effectiveness of 3D CA approach is demonstrated by studying the extension of a single dendritic grain in a squared platform under various conditions [2-7].

Both 2D decentered square and 3D decentered octahedron CA growth algorithms were presented and have been validated against the predictions of 9 analytical models. When applied to the study of the extension of a single dendritic grain in a rectangular platform, the 3D CA model demonstrated its ability to account for different cooling conditions, crystallographic orientations and growth kinetics parameters. Although they require the definition of a virtual growth center, these algorithms are effective in required computational time. The 3D CA calculation of the octahedral grain was performed (650 time step, domain containing 1 million cells-100 x 100 x 100) in 180 s on a Hewlett-Packard 735 workstation when defining the neighborhood of the cells with the first nearest neighbors (six neighbors). In fact, it should be noted that a correct prediction of the growth competition between two columnar grains requires the use of a second order neighborhood of the cells in the 2D CA model (eight neighbors in a square lattice). In the 3D CA model, an extension to a higher neighborhood is also expected to be required for modelling the competition between columnar grains. Such an extension will increase the CPU time [2-7].

V. Abramov and team contributed significant work to the field of ultrasonic application for reduction in mean grain size, variation in phase distribution and better material homogeneity and separation control [2-8]. In one of their experiments on solidification of aluminum alloys under ultrasonic irradiation using water-cooled resonator; it was revealed that ultrasonic treatment can be applied to almost all aluminum alloys since the elongation values of ultrasonic-treated specimens was much higher than those of non-treated. The schematic diagram of the ultrasonic apparatus is shown in Figure 2.10.

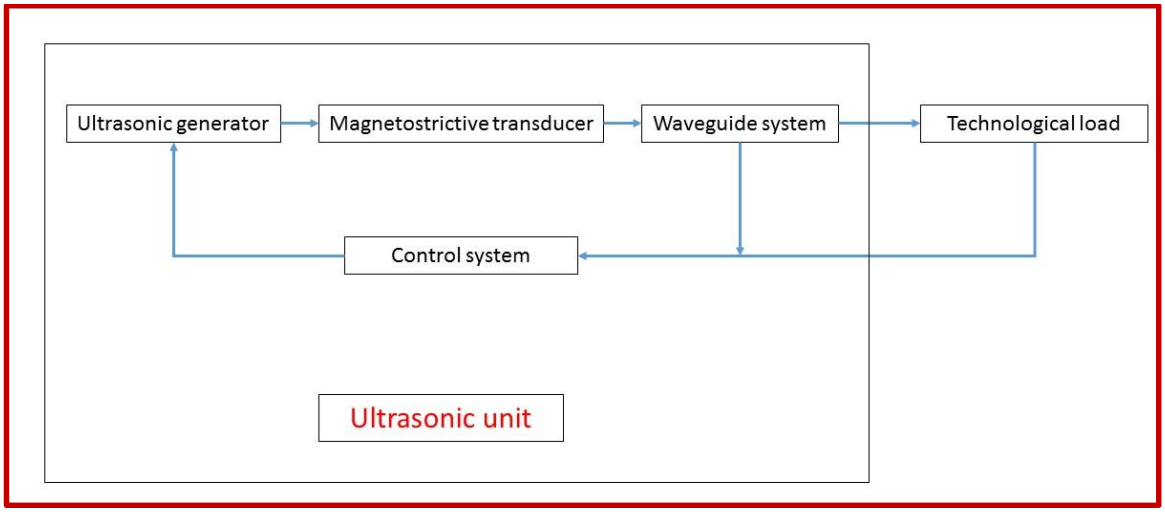

Figure 2.10: Schematic diagram of ultrasonic unit [2-8]

It was also determined that pure metals have poorer ultrasonic treatability, as pure aluminum could not be effectively treated. Their experimental setup involves a water cooled Mode Transformation System (MTS), magnetostrictive transducer and ultrasonic generator, of which the transducer and ultrasonic generator are immersed into the molten metal pool in a crucible of 80 mm diameter and 160 mm height. It was observed that there is a 35% improvement in tensile strength in ultrasonically treated material, the hardness increased by 14% and an increased elongation of 52% [2-8].

2.3. Rapid Solidification

Enrique J. Lavernia and T. S. Srivatsan worked on a review article focused on the rapid solidification processing of materials and categorized the rapid solidification process as shown in Figure 2.11[2-9].

Process name	Description	Product/dimensions	Cooling rate ($K\ s^{-1}$)
Atomization methods			
Fluid atomization (normally twin jets)	High-pressure fluid impacting a continuous stream of liquid metal	For gas : low O_2 contamination Spherical and smooth powder 50/100 μm dia	Gas: 10^2–10^3 SSGA: up to 10^6
Gas (Ar, N_2)	Ultrasonic G.A: disintegration occurs by high intensity pulsed waves	Supersonic G.A: 10–50 μm Ultrasonic G.A: <30 μm	USGA: 10^5
Water		For water: high O_2 contamination Irregular particulates 75/200 μm dia	Water: 10^2–10^4
Vacuum atomization (soluble gas)	Molten metal supersaturated with gas under pressure is suddenly exposed to vacuum, gas expands causing liquid to atomize	Spherical powder 40/150 μm dia	10^4–10^5
Drum splat quenching	Gas atomized droplets directed to impinge on a rotating drum	Flakes 50/100 μm thick 1–3 mm dia	10^4–10^5
Rotating electrode process (REP)	Alloy in electroded form is rotated (250 rps) while being melted by an arc plasma/bean. Molten metal is ejected centrifugally and solidified in an inert gas filled chamber	Spherically/smooth powder 150/200 μm dia	10^2
Rapid solidification rate (RSR) (centrifugal atomization)	Molten metal is ejected into a rotating water-cooled cup/ disc resulting in fine droplets cooled by high flow helium gas	Spherical powder <100 μm dia	10^5
Twin roll atomization	Mechanical atomization process where stream of molten metal is directed into a high speed contra rotating rolls	Variable powder/flake 200 μm thick	10^5–10^6
Laser melting/spin atomization	Focused (CO_2) laser beam is used to melt the top of the rotating rod. Droplets are expelled by the centrifugal force and cooled by the inert gas	Spherical particles 40 μm dia	$\geq 10^6$
Electrohydrodynamic atomization (EHDA)	Electric field is applied to the surface of liquid metal and causes a droplet to be emitted	Droplets > 0.01–150 μm dia	10^7
Spark erosion technique	Repetitive spark discharge between two electrodes immersed in a dielectric fluid. Spark vaporizes a small amount of metal that immediately freezes	≥0.5 μm dia contamination from dielectric fluid	10^5–10^6
Electron bean meting combined with spat quenching (EBSQ)	A focused electron beam melts the bottom tip, molten drops fall onto the surface of a rotating disc	Flakes 50 mm dia 50 μm thick	10^6
Chilling methods			
Melt spinning (CBMS)	Molten metal is expelled out onto a rotating wheel (flat or notched)	Ribbons thick 25/50 μm	10^5–10^7
Crucible melt extraction (CME)	Molten metal solidifies on the edge of a water-cooled disc and flies off	Filaments or fibers 20–100 μm thick	10^5–10^6
Melt drag (overflow)	Overflow of a molten metal from a reservoir onto a chill rotating surface	Filaments, foils, particulates	10^4–10^6
Pendant drop (POME)	Filament is extracted from molten end of a rod suspended just above the rotating wheel	Filaments, fibers	10^5–10^6
Rapid spinning cap (RSC)	Stream of molten metal is ejected onto a thick layer of rotating liquid located in the interior wall of a spanning cup	Spherical to irregular powder/flakes 50 mm dia 50 μm thick	10^6
Plasma and anvil twin pistons	Droplet of molten metal is impacted by pistos(s)	Splat 5–300 μm thick	10^4–10^6
Plasma spray deposition	Molten metal is propelled onto a substrate by a hot ionized gas emanating from the plasma torch. If deposited layers are kept very thin, rapid solidification is possible. Potential for near net shape. Coherent deposit	Porous layer >50 μm thick	10^3–10^6
Arc spray	Electrically opposed charged wires of the alloy to be sprayed are fed together to produce a controlled arc. The molten metal is atomized and by a stream of gas is projected onto a substrate	Porous film >50 μm thick	10^2–10^3

Figure 2.11: Rapid solidification techniques [2-9]

S.A. David and his team investigated the effect of rapid solidification on microstructures in stainless steel weld and its implications on the Schaeffler Diagram as shown in Figure

2.12 and found that both weld pool cooling rate and post solidification solid-state cooling rates have a significant effect on the microstructures [2-10].

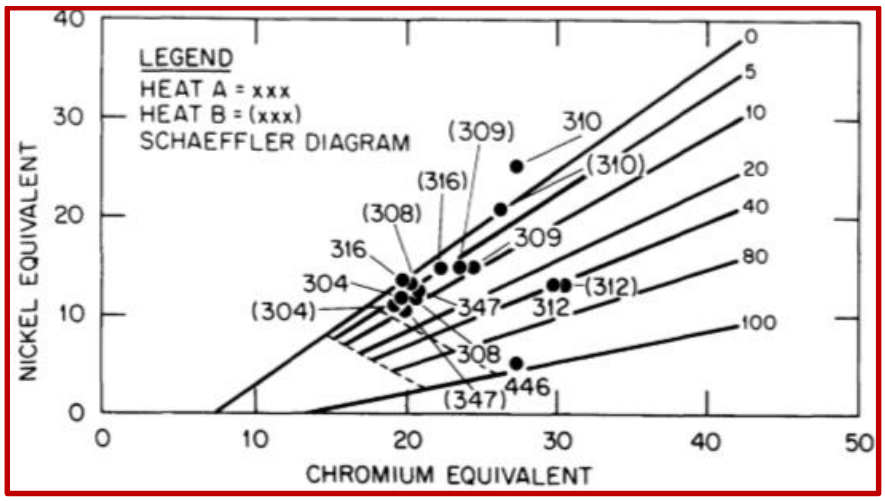

Figure 2.12: Scheaffler diagram of Steel samples [2-10]

The microstructures ranged from duplex austenite (7") + ferrite (6) to fully austenitic or fully ferrite. It was found that the microstructures were influenced by both cooling rates and composition. Different compositions of stainless steel were laser welded at different speeds and laser power levels. Electron diffraction technique was used to characterize phase distribution. It was observed that the weld pool cooling rate and post-solidification solid state cooling rates have a considerable impact on the resulting microstructures. It was also noted that welding would fall under the rapid solidification category and varying welding speeds result in different cooling rates. The microstructures of 316A laser welds at a) 12.7 cm/min, b) 50.8 cm/min, c) 190.5 cm/min and 316B laser welds at d) 12.7 cm/min, e) 50.8 cm/min and f) 190.5 cm/min are as shown in Figure 2.13 [2-10].

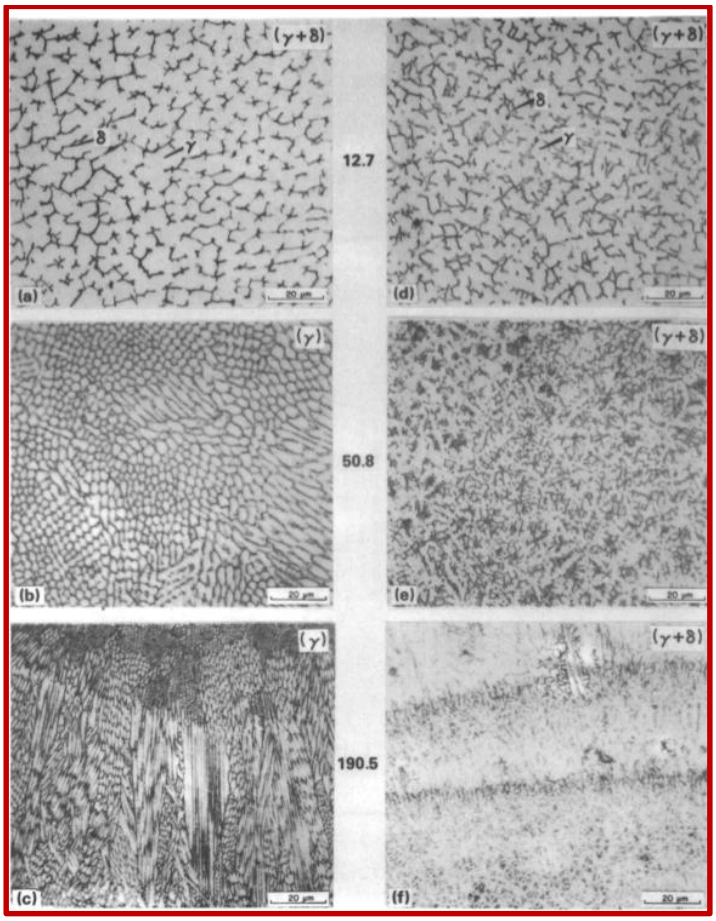

Figure 2. 13: Microstructures of 316A and 316B laser welds [2-10]

2.4. Application of Ultrasonics in AM

Ultrasonic Additive Manufacturing (UAM) invented and patented by Dr. Dawn white combines ultrasonic welding (USW) and CNC machining to join metal foils layer by layer. The energy generated from the transducer through a sonotrode to the work piece in the form of ultrasonic oscillation. The interlaminar metal flow with associated localized heating result in the solid state bonding is generated by the oscillations and compressive normal force of the sonotrode. The traditional UAM process utilizes a 1kW seam welder as a standard USW system and was developed to a higher power 9kW in 2008 by Solidica Inc. partnered with Edison Welding Institute (EWI). It is used to process high

strength aluminum alloys e.g. 2024, 7075; 316 SS and copper. As with most AM techniques, UAM can produce complex internal channels and voids which can be applied for complex thermal management applications like the microchannel cooling. Because of the solid state joining of the components, dissimilar material bonding can be achieved unlike other AM processes. Object embedment is also accommodated by UAM, in which active, passive, optical fibers and other required components are embedded into Al matrix because of low temperature and high plastic flow that can occur in the material during ultrasonic excitation [2-11].

One of the major applications of AM is in the medical field and also in several post processing techniques. Ben Vandenbroucke and Jean-Pierre kruth worked on Selective Laser Melting (SLM) of biocompatible metals for rapid manufacturing of medical parts manufactured with titanium and cobolt-chromium and used glass blasting and ultrasonic ceramic filling as post processing techniques and measured the surface roughness on the top and side surfaces of the titanium and cobolt-chromium SLM samples and are as shown in Figure 2.14 [2-12].

	SLM Ti-6Al-4V		SLM Co-Cr-Mo	
	Top	Side	Top	Side
As Processed				
R_a (µm)	18		15	15
R_z (µm)	92		87	90
Glass blasted				
R_a (µm)	12		12	8
R_z (µm)	70		66	43
Ultrasonic ceramic filed				
R_a (µm)	10		7	5
R_z (µm)	45		40	25

Figure 2.14: Top and Side surface roughness [2-12]

2.5. Summary:

As it can be observed from the past work, most of it either involves the immersion of the ultrasonic unit into the molten metal pool, which damages the horn that is immersed or the use of expensive equipment and processes. The equipment cost increases as the horn has to be replaced for each production run. It is important to develop an alternative approach, which is affordable and by which the same or nearly similar results can be achieved by ultrasonic treatment without actually damaging the equipment. Further, such an approach can be integrated with AM where rapid solidification is pre-dominant (due to dissimilar thermal gradient) along the build direction.

References:

2-1 John. A. Slotwinski, Edward J. Garboczi, and Keith M. Hebenstreit, 2014, "Porosity Measurements and Analysis for Metal Additive Manufacturing Process

Control", Journal of Research of the National Institute of Standards and Technology, Volume 119

2-2 David, Gill, " Laser Engineering Net Shaping", URL: http://www.sandia.gov/mst/pdf/LENS.pdf June 24th 2015 accessed

2-3 Ehsan foroozmehr, Dechao Lin, Radovan kovacevic',2009, "Application of vibration in the laser powder deposition process", Journal of Manufacturing Processes 11, 38–44

2-4 Longbiao He, Minsheng Wu, Luming Li, and Hongwei Hao , 2009, "Ultrasonic generation by exciting electric arc: A tool for grain refinement in welding process", Journal of Manufacturing Processes 11, 38–44

2-5 Jafarr Saniie and Nihat M. Bilgutay, 1986, "Quantitative grain size evaluation using ultrasonic backscattered echoes", J. Acoust. Soc. Am. 80 (6)

2-6 Ch.-A. Gandin and M. Rappaz, 1997, "A 3D Cellular Automaton Algorithm for The Prediction Of Dendritic Grain Growth", Acta mater. Vol. 45, No. 5, pp. 2187-2195

2-7 V. Abramov, O. Abramov, V. Bulgakov, F. Sommer, 1998, "Solidification of aluminum alloys under ultrasonic irradiation using water-cooled resonator", Materials Letters 37, 27–34

2-8 Enrique J. Lavernia, T. S. Srivatsan, 2010, "The rapid solidification processing of materials: science, principles, technology, advances, and applications", J Mater Sci 45:287–325

2-9 S. A. David, J. M. Vitek, R. W. Reed, and T. L. Hebble, “Effect Of Rapid Solidification On Stainless Steel Weld Metal Microstructures And Its Implications On The Schaeffler Diagram”, ORNL/TM-10487

2-10 Juan A. Gallego Juarez and Karl F. Graff , 2014, “Power Ultrasonics: applications of high-intensity ultrasound”, Elsevier

2-11 Ben Vandenbroucke and Jean-Pierre Kruth, “Selective laser melting of biocompatible metals for rapid manufacturing of medical parts” , Rapid Prototyping Journal, Vol. 13 Iss 4 pp. 196 - 203

Chapter 3: Materials and Methodology

In this chapter, the experimental setup and methodology used in this research are discussed. The experimental setup involves employing a low cost metal 3D printer originally developed by Joshua M. Pearce and his team at Michigan Technological University and an ultrasonic transducer setup developed in Center for Innovation in Additive Manufacturing (CIAM) at Youngstown State University. The ultrasonic setup to induce vibration during deposition includes a 50 kHz ultrasonic transducer, digital multimeters, control driver for ultrasonic transducer and a transformer to vary the power input to the transducer. The materials involved in the construction of each component are also explained in this chapter.

3.1. Experimental Setup

3.1.1. Low Cost Metal 3D Printer:

The basic components of the low cost metal 3D printer as shown in Figure 3.1 are:

1. Frame
2. Carriage
3. Welder mount
4. Effector plate and mounts
5. Magnetic bearings
6. MIG welder

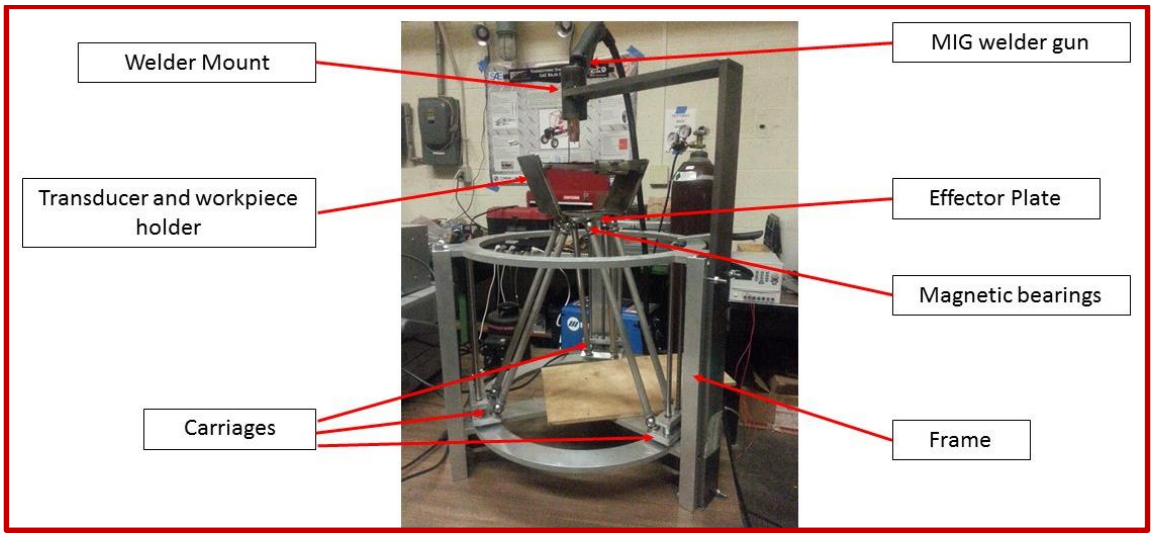

Figure 3.1: Low-Cost Metal 3D Printer

The effector plate which fixtures the transducer and workpiece holder is supported by the frame connected to magnetic bearings present at both the bottom end of the effector plate and top end of the carriages. The carriages are mounted on the lead screw of the stepper motor and are supported on either side using support rods. The frame supports the entire assembly, including the mounted weld head, in this case, a Millermatic 140 Autoset with an input power of 115 V- 20 A welder.

The CAD model of the 3D printer designed by Michigan Technological University is shown in Figure 3.2.

Figure 3.2: Solidworks model of 3D metal printer [Source: Dr. Joshua Pearce, Michigan Tech University, 3-1]

All the components of the metal 3D printer except for the magnetic bearings are machined using water jet cutting.

The printer is driven using an Arduino Mega 2560 motherboard as shown in Figure 3.3 with a 12v input voltage and uses Repetier software. Marlin firmware is used with customization for the inverted delta construction using Arduino software, by inverting the functions for the base plate movement and stepper motor. The Arduino Mega 2560 is also compatible with LCD display panels and advanced heat sensing applications, which are additional capabilities that can be integrated with this 3D printer.

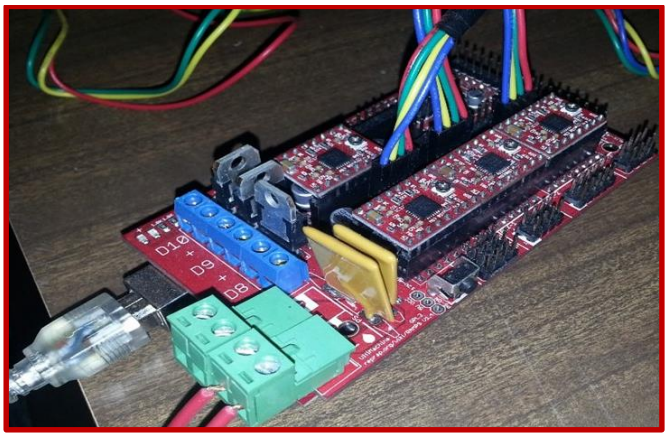

Figure 3.3: Arduino Mega 2560 Motherboard

As shown in Figure 3.4, the open source Repetier and Marlin firmware used for generating G-code, controls and interfacing with the metal 3D printer can be customized according to the demand and the functionality required e.g. #define BAUDRATE, #define DEFAULT_AXIS_STEPS_PER_UNIT.

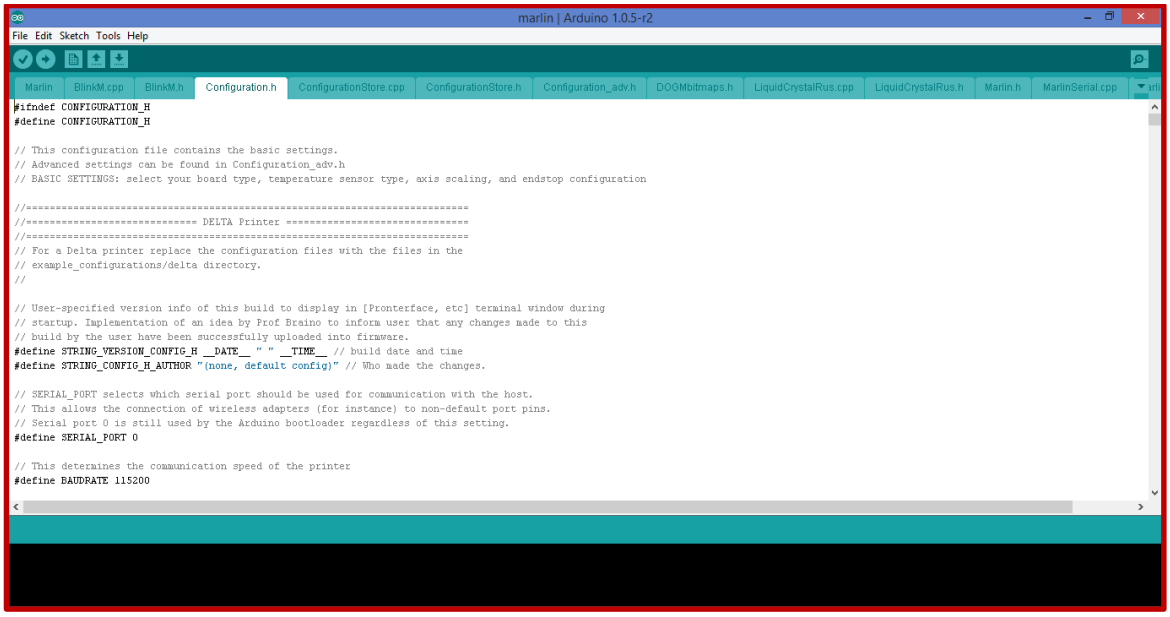

Figure 3.4: Arduino software interface

The changes required in the configuration file would involve defining the work envelope of the printer, the stepper motor configuration and defining the coordinate system that the

3D printer should follow, depending on the type of construction of the 3D printer e.g. Deltabot, Inverted delta etc.

3.1.2. Ultrasonic Transducer:

A focused contact type piezoelectric transducer with an active area of 50 mm diameter and nominal frequency of 50 kHz is used for the experiment. It is capable of handling a voltage peak to peak of 1000Vpp. The horn is made of polystyrene. The transducer is shown in Figure 3.5.

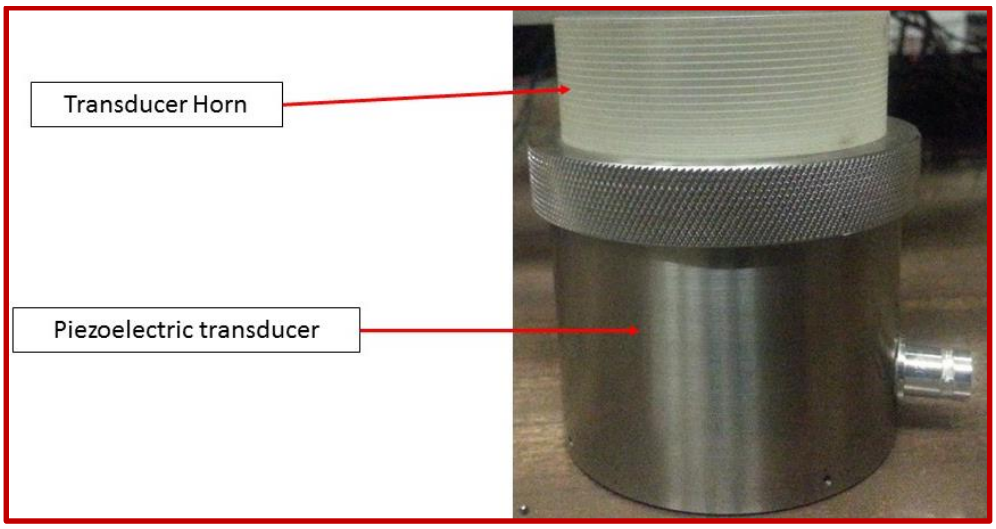

Figure 3.5: Ultrasonic transducer

3.1.3. Transducer and Workpiece Holder:

In order to maintain uniform deposition and to focus vibration on the spot of deposition, it is essential to hold both the transducer and work piece at the same area. In order to achieve this, a holder which fits within the metal printer is fabricated as shown in Figure 3.6. It also helps to avoid interference of ultrasonic waves with the Arduino Mega 2560 board.

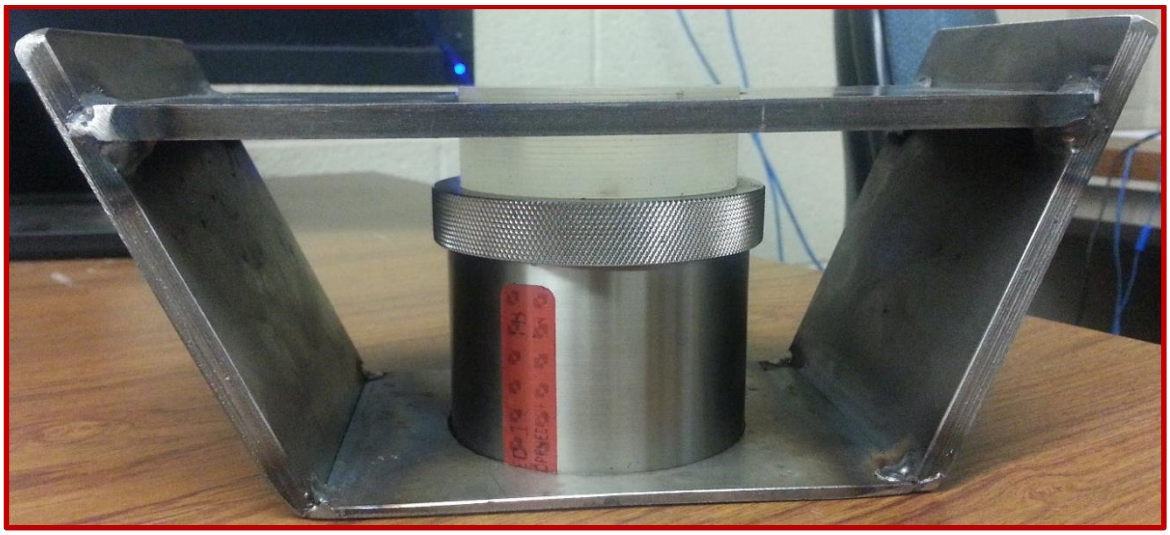

Figure 3.6: Transducer and work piece holder

3.1.4. Transducer Driver

The driver consists of a variable DC power supply, dead time generation circuitry for forming non-overlapping “high” and “low” signals from the input pulse signal, a high and low side driver, and a half-bridge circuit constructed using identical N-channel MOSFETs. The power supply is a rectified and filtered sine wave from a variac plugged into a 120 V wall outlet. The variac is used to adjust the amplitude of the voltage signal applied to the transducer. A function generator (Agilent 33220A) is set to generate a pulse signal (0 - 5 V) at a certain frequency, which is applied as an input to the driver. The frequency of the pulse signal will control the frequency of the voltage signal applied to the transducer. The pulse signal is fed into the driver circuit via an optocoupler with a Schmitt trigger output (Fairchild Semiconductor H11L1V-M). The output of the optocoupler provides input to the dead time generation circuitry. This circuitry is used to guarantee that the high and low voltage signals applied to the transducer do not overlap,

which would form a short circuit and damage the driver. The circuitry uses nor gates and low pass filters to create two non-overlapping pulse signals, which provide input to the high and low side driver chip (International Rectifier IR2110PBF). The driver chip provides signals to the half bridge, which turn on the appropriate MOSFETs according to the pulse signals generated by the dead time generation circuitry. The half bridge switches power to the transducer from the positive or negative side of the DC power supply.

The output voltage and current are monitored by measuring the voltage drops across certain resistors in the driver circuit. These were measured using Agilent 33401A multimeters. The circuit is capable of driving the transducer at 200 V (p-p) at up to 1 A (rms) and frequencies from 1 Hz to 1 MHz. The circuit of the driver is as shown in Figure 3.7 and 3.8.

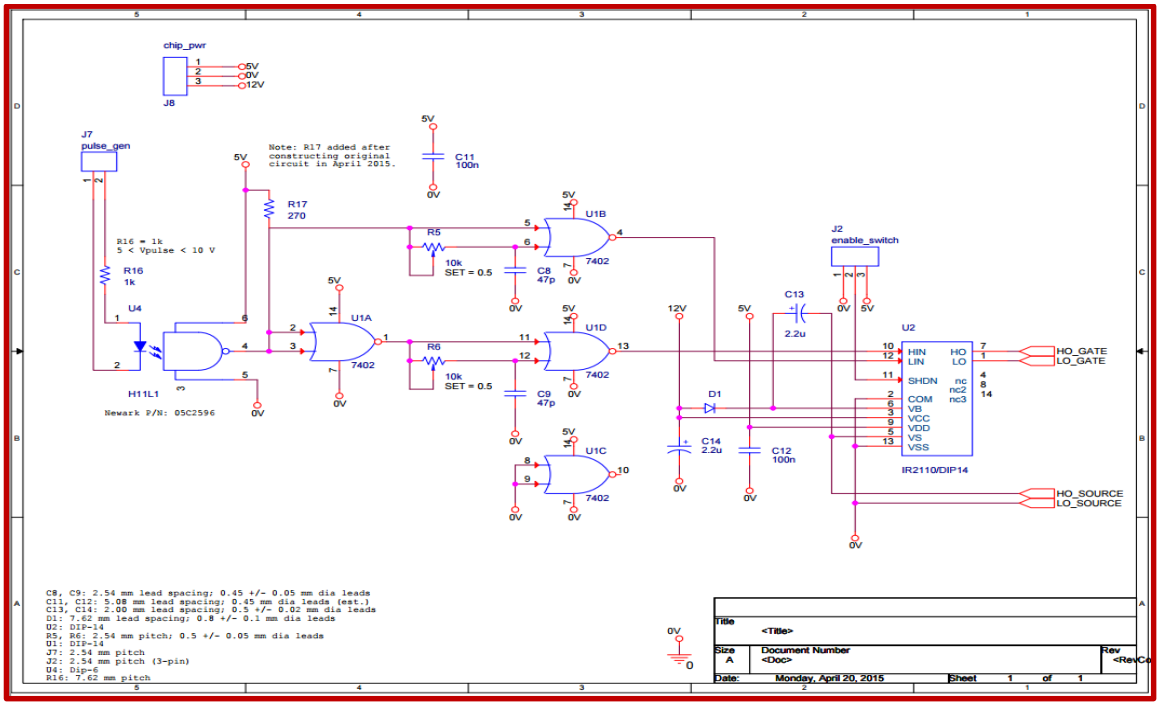

Figure 3.7: Transducer Driver Circuit

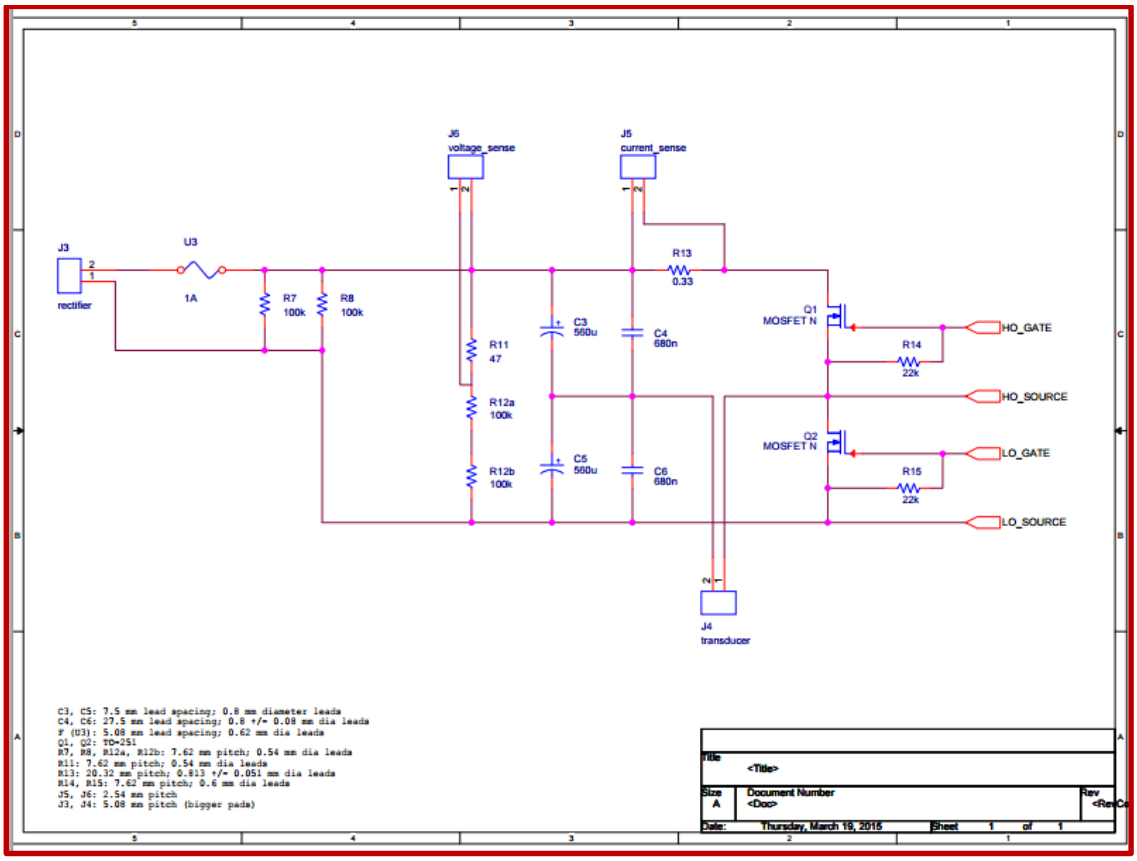

Figure 3.8: Driver Circuit (continued)

Two Agilent 34401A Digital Multimeters are used to measure the voltage and current input and a frequency modulator to input different frequencies are attached to the transducer.

An Agilent oscilloscope image as shown in Figure 3.9 is acquired to determine the ideal vibration frequency to be used in this study and 38 kHz was determined to be ideal.

The resistance values from R13, R11, R12a and R12b as shown in Figure 3.8 are used for power calculations

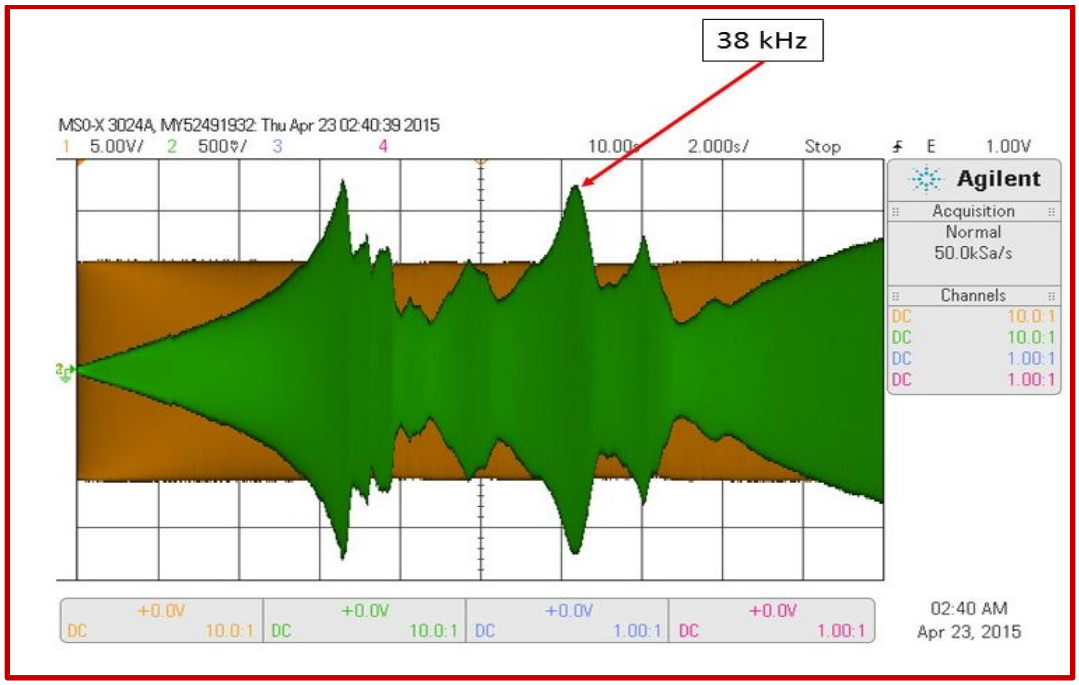

Figure 3.9: Oscilloscope image

3.2. Methodology

3.2.1. Weld Bead Deposition

The Arduino board is connected to a 12v power supply and also to the USB port of the computer. The ultrasonic transducer which is connected to the digital multimeters and transformer is placed inside the holder and connected to the driver. The holder is held in place with a magnetized base. The arrangement of the equipment is as shown in Figure 3.9.

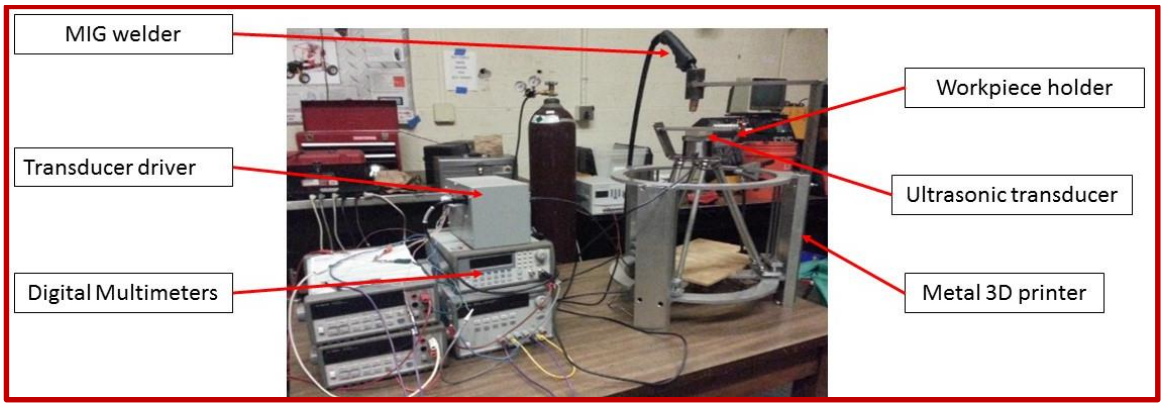

Figure 3.10: Experimental setup

ER70S-6 material is a mild steel material with a chemical composition Si - 0.80-1.15% Mn - 1.4-1.85% P - 0.025% C - 0.06-0.15% S - 0.035%, commonly used for welding is deposited using a Millermatic 140 Autoset on a 1/8" plate at a feed rate of 45 ipm.

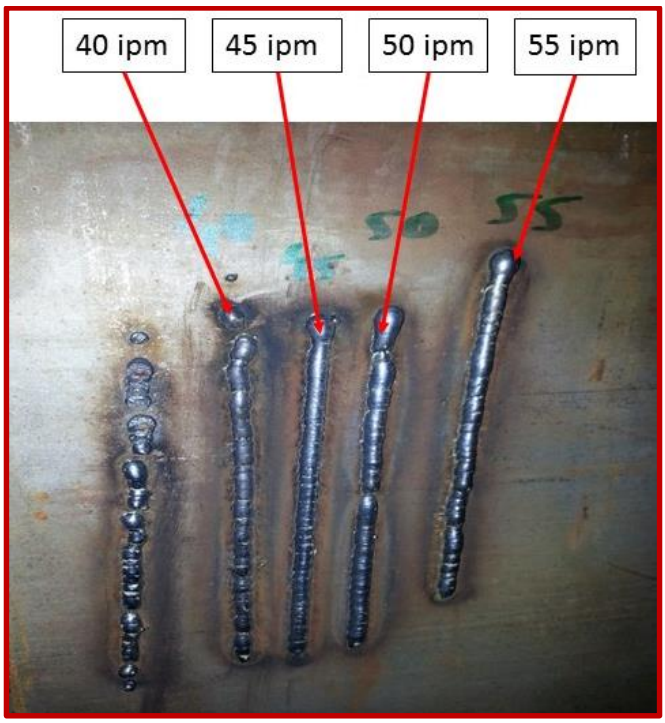

Figure 3.11: Weld bead selection

As it can be seen in the above Figure 3.10, 45 ipm was the ideal feed rate with the current setup to achieve a good quality weld bead. The G-code for the printer allows the weld

gun to deposit in the area in contact with center of the transducer horn. The plate used for deposition is 1018 cold rolled SS plate with a thickness of 1/8". Before depositing the material on a SS plate, while the plate was being vibrated ultrasonically, the digial multimeters were powered to 5 Vpp and the required frequency settings were preset, before activating the driver and transformer. Three frequency settings were considered i.e. 20 kHz, 38 kHz and 56 kHz at two different transformer settings i.e. at 50% capacity and 100% power capacity. Three weld beads per frequency per power settings were deposited.

3.2.2. Sample Preparation

Upon deposition, the samples were cut in the longitudinal direction (w.r.to deposition direction) from the middle of the bead using a band saw. The samples were then ground and polished using the Streurs polishing plates with the procedures shown in Tables 3.1 and 3.2

Table 3.1: Grinding

Grinding	Plane Grinding	Fine Grinding 1
Disc/Cloth	MD-Piano	MD-PLAN
Grit/Grain Size	220	9μm
Abrasive	diamond	diamond
Abrasive Dosing	---	3
Speed (rpm)	300	150
Applied Load (N)	30	30
Lube	H_2O	Green

Grinding	Plane Grinding	Fine Grinding 1
Lube Dosing	---	7
Time	as needed	5 min.

Table 3.2: Polishing

Polishing	Diamond Polishing 1	Diamond Polishing 2	Oxide Polishing
Disc/Cloth	MD-DAC	MD-NAP	MD-CHEM
Grain Size	3μm	1μm	0.04μm
Abrasive	diamond	diamond	OP-U
Abrasive Dosing	3	3	7
Speed (rpm)	150	150	150
Load/spc. (N)	30	30	30
Lubricant	Green	Green	---
Lube Dosing	7	9	---
Time	4 min.	2 min.	1 min.

As indicated in the tables, the first step was the mechanical material removal (grinding) in which non-planar sections caused by band saw are removed. Plane grinding was performed in order to ensure that the surfaces of the sample are flat and similar. Fine grinding produced the surfaces with deformations small enough to be removed by the polishing. The diamond polishing disc and abrasive suspended oxide solution were used to achieve the best possible planeness for optimum quality [3-2].

The obtained mirror finished sample is etched in 2% Nital, which is a combination of ethyl alcohol and nitric acid.

3.2.3. Optical Microscopy and Image processing:

A Zeiss Axiophot optical microscope as shown in Figure 3.11 is used to acquire the microstructural images at 5X, 10X and 20X focus.

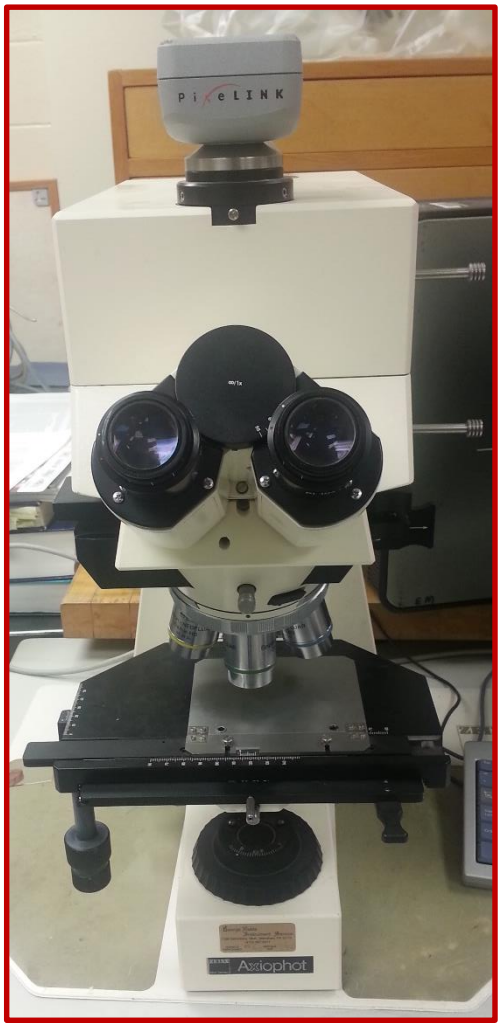

Figure 3.12: Zeiss Axiophot Optical Microscope

ImageJ is an open source Java image processing program with capabilites to display, edit, analyze, process, save and print 8-bit, 16-bit and 32-bit images. It supports standard

image processing functions such as contrast manipulation, sharpening, smoothing, edge detection and median filtering. This program was selected for image processing as it allows the user to calculate area and pixel value statistics along with image processing tools (e.g. noise filtering tools) for microstructure analysis [1]. ImageJ is used in this study to determine the average grain size and the count of the grains to determine the impact of ultrasonics on the microstructures.

The sequence of steps that were followed in the image processing and analysis as shown in Figure 3.12:

a) Cropping the image by specifying a standard selection area
b) Applying the background correction plugin, which does the pixel modulation, threshold control, brightness and contrast correction
c) Converting the image to binary and inverting it
d) Removing the extra noise using the despeckle and median filter with a 1.5-2 pixel radius
e) Use the watershed and analyze particles with the area selection from 1000μm^2-infinity and circularity from 0 (e.g. straight line) to 0.9 (almost circular profile)
f) The obtained results are then exported to Microsoft excel
g) Analysis on grain size, counts and correlation to vibration conditions are performed

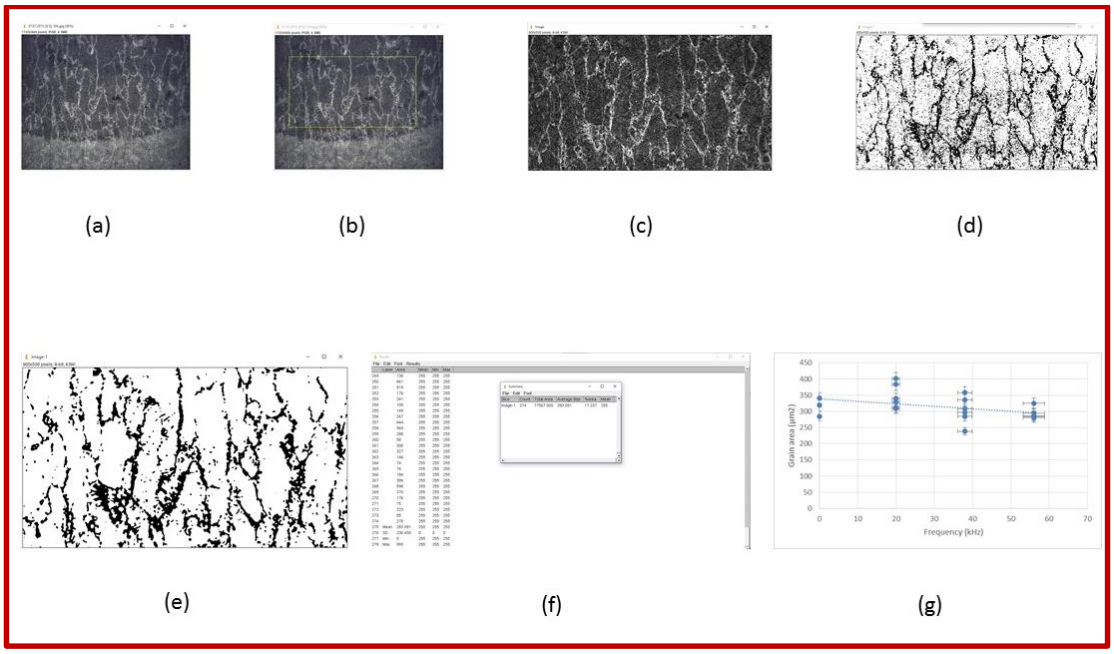

Figure 3.13: Image processing and analysis using imageJ. a) Image from optical microscope; b) Selection box; c) Background corrected; d) Binary image; e) Noise adjusted; f) Report generation; g) plots

3.2.4. Microhardness Testing:

Microhardness testing was performed using a NANOVEA M1 Hardness tester as shown in Figure 3.13 and two sets of data were collected for both weld bead and heat effected zone for each sample.

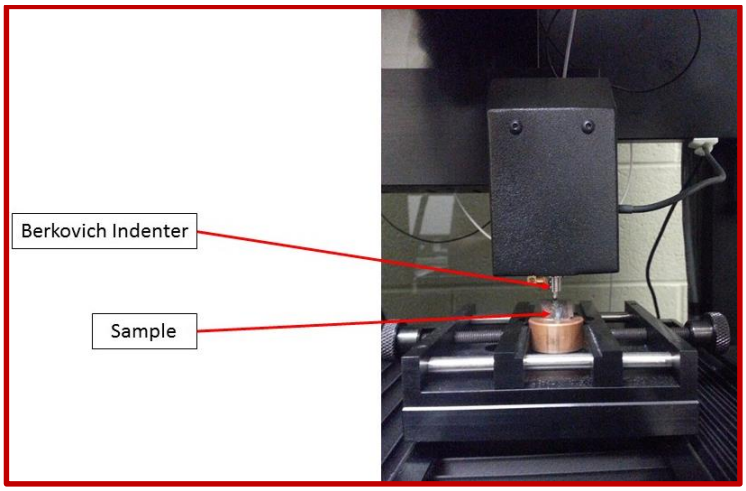

Figure 3.14: NANOVEA M1 Hardness tester

Hardness test was performed using the Berkovich indenter and an example of the measuring report is shown in Figure 3.14.

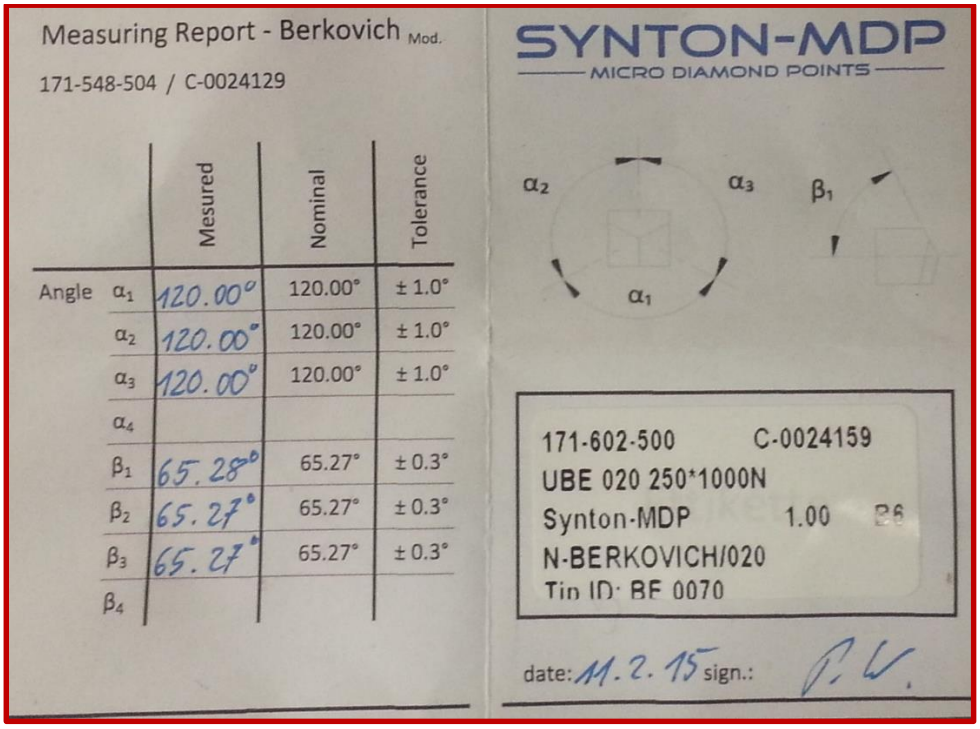

Measuring Report - Berkovich Mod.

171-548-504 / C-0024129

		Mesured	Nominal	Tolerance
Angle	α_1	120.00°	120.00°	± 1.0°
	α_2	120.00°	120.00°	± 1.0°
	α_3	120.00°	120.00°	± 1.0°
	α_4			
	β_1	65.28°	65.27°	± 0.3°
	β_2	65.27°	65.27°	± 0.3°
	β_3	65.27°	65.27°	± 0.3°
	β_4			

SYNTON-MDP
MICRO DIAMOND POINTS

α_2 α_3 β_1 α_1

171-602-500 C-0024159
UBE 020 250*1000N
Synton-MDP 1.00
N-BERKOVICH/020
Tip ID: BF 0070

date: 11.2.15 sign.:

Figure 3. 15: Measuring report of Berkovich indenter

Following are the sequence of steps involved in the microhardness testing on the NANOVEA M1 hardness tester:

1) Load the sample on to the platform, which is mounted on the anti-vibration pneumatic vibration isolation table.
2) Indenter information module saves the indenter details such as α and β values
3) Start the stage control module of the Nano indentation program
4) Move the stage under the indenter, so that the region of interest is under the indenter and auto contact the indenter using the stage controller software
5) Start new test and input the load of 300mN, loading and unloading rate of 160mN/min and creep (time for indenter to load after 300mN force is achieved) of 15 seconds to start the test
6) After the test is complete, the reports with all the hardness test analysis are generated

ASTM E2546 standards are followed by NANOVEA software to calculate hardness and elastic modulus form the load-displacement curve as shown in Figure 3.15 [3-3].

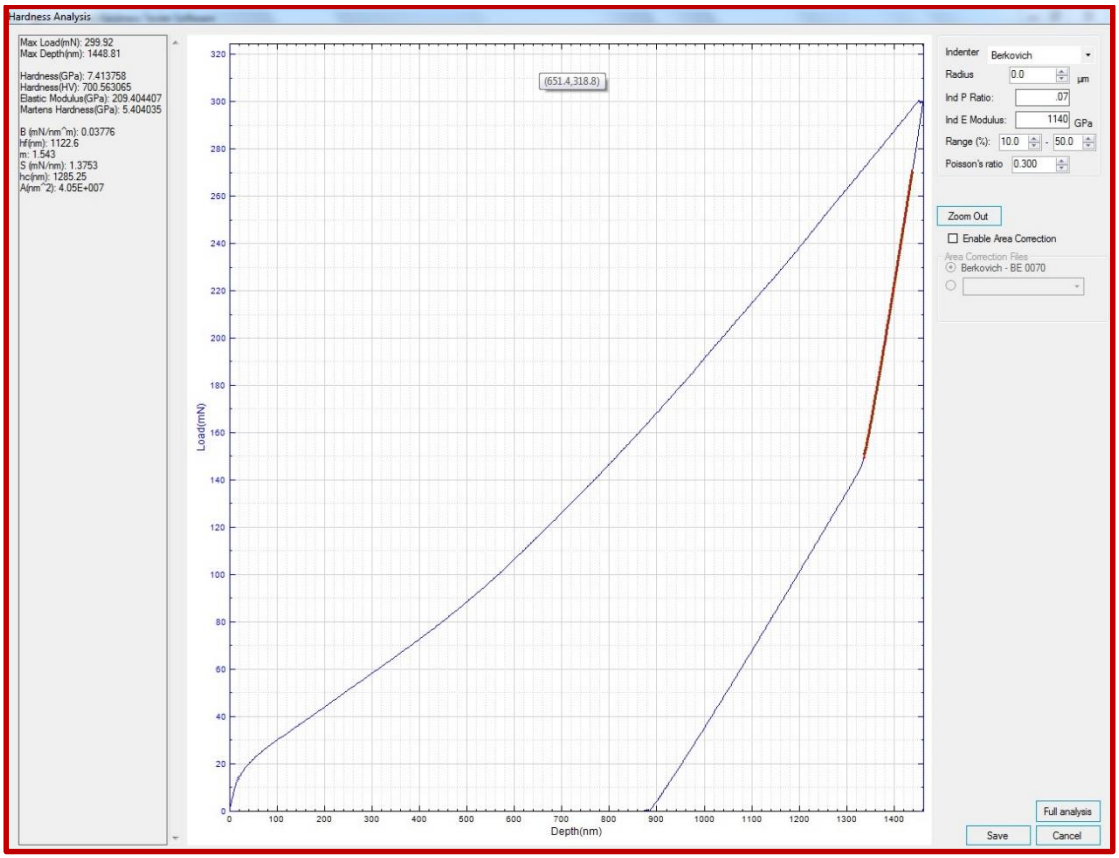

Figure 3.16: Load- Displacement curve

The area function for a Berkovich indenter is

$$A_c=24.5hc^2 \tag{3.1}$$

where h_c is the contact depth and is calculated using

$$hc = hmax - \frac{3* Pmax}{4*S} \tag{3.2}$$

Where hmax, Pmax and S are derived from the curve and are maximum contact depth, maximum load and slope respectively [3-3].

The hardness is calculated using

$$H = \frac{Pmax}{Ac} \tag{3.3}$$

For Young's modulus calculation, the reduced modulus is given as

$$Er = \left(\frac{\sqrt{\pi}}{2}\right) * \left(\frac{S}{\sqrt{Ac}}\right) \tag{3.4}$$

$$\frac{1}{Er} = \left(\frac{1-V2}{E}\right) + \left(\frac{1-*Vi2}{Ei}\right) \tag{3.5}$$

Where *E*i and *V*i are the Young's modulus and Poisson's ratio of the indenter and *V* is the Poisson's ratio of the tested sample.

Null hypothesis statistical techniques called ANOVA two factor with replication and single factor analysis were used to determine the impact of both power and frequency on the microstructures and hardness.

3.3. Summary:

In summary, this chapter detailed the construction of the experimental setup, sequence of steps involved in the weld bead deposition, sample preparation, image acquisition using optical microscopy, processing and analysis using ImageJ, statistical analysis using ANOVA to determine the impact of power and frequency of the ultrasonic transducer on the microstructures and hardness.

References:

3-1 Wayne Rasband, "Introduction", URL: http://imagej.nih.gov/ij/docs/intro.html, June 13th 2015 accessed

3-2 Struers, "Products", URL: http://www.struers.com/default.asp?top_id=3&doc_id=282 , August 3rd accessed

3-3 Duanjie Li, Pierre Leroux , 2014, “Yield & Tensile Strength Of Steel & Aluminium Using Microindentation”, Nanovea, California

Chapter 4: Results and Analysis

In this chapter, the data obtained from ImageJ and Nanovea hardness testing machine are presented and analyzed. The chapter is sub divided into three categories, namely Power calculations, which explains how energy input through vibration is collected from the multimeters and converted to power; Microstructure analysis, which explains the analysis of data obtained from the optical imaging and analysis software, ImageJ, and finally, Microhardness analysis, which explains the analysis of Vickers hardness testing. ANOVA analysis is used in order to find the statistical integrity of the data and also determine the influence of ultrasonic waves on grain structures. Also, a summary of the results and observations are presented.

4.1. Power Calculations:

Two transformer settings were used in generating two different power conditions each for the three conditions used: no power, low power and high power, for the transducer at individual frequencies of 20 kHz, 38 kHz and 56 kHz respectively. This power modulation is achieved with a controller present on the top of transformer powering the transducer. The power levels utilized are shown in Table 4.1. The samples created with the controller position 1 will be named Low Power (LP) and for the controller position 2 High Power (HP) and the three frequencies will be named Low Frequency (LF), Medium Frequency (MF) and High Frequency (HF). The control samples created without vibration are named No Vibration (NV).

Table 4.1: Frequency and Power

Frequency (kHz)	Controller Position 1 (W) LP	Controller Position 2 (W) HP
20 (LF)	3	4.57
38 (MF)	10.65	19
56 (HF)	16.56	30.83

The power calculations are performed using the equations 4.1, 4.2 & 4.3

$$I = Vac/0.33 \tag{4.1}$$

$$V = Vdc * (\frac{200047}{47}) \tag{4.2}$$

$$P = V * I \tag{4.3}$$

The *Vac* and *Vdc* values were obtained from the digital multimeters.

The design of experiments involving three trials selected for this study is shown in Table 4.2.

Table 4.2: Design of Experiments

Power (W)	Frequency (kHz)	Sample
0	0	NV S1, NV S2, NV S3
LP	LF	20 LP S1, 20 LP S2, 20 LP S3
LP	MF	38 LP S1, 38 LP S2, 56 LP S3
LP	HF	56 LP S1, 56 LP S2, 56 LP S3
HP	LF	20 HP S1, 20 HP S2, 20 HP S3
HP	MF	38 HP S1, 38 HP S2, 56 HP S3
HP	HF	56 HP S1, 56 HP S2, 56 HP S3

The experiment was performed in the following order:

1. HP LF
2. HP MF
3. HP HF
4. LP LF
5. LP MF
6. LP HF

4.2. Microstructure analysis:

Some of the microstructure images obtained from the optical microscopy mentioned in Chapter 3 are as shown in Figures 4.1-4.4.

Figure 4.1: NV S3

Figure 4.2: 20 LP S1

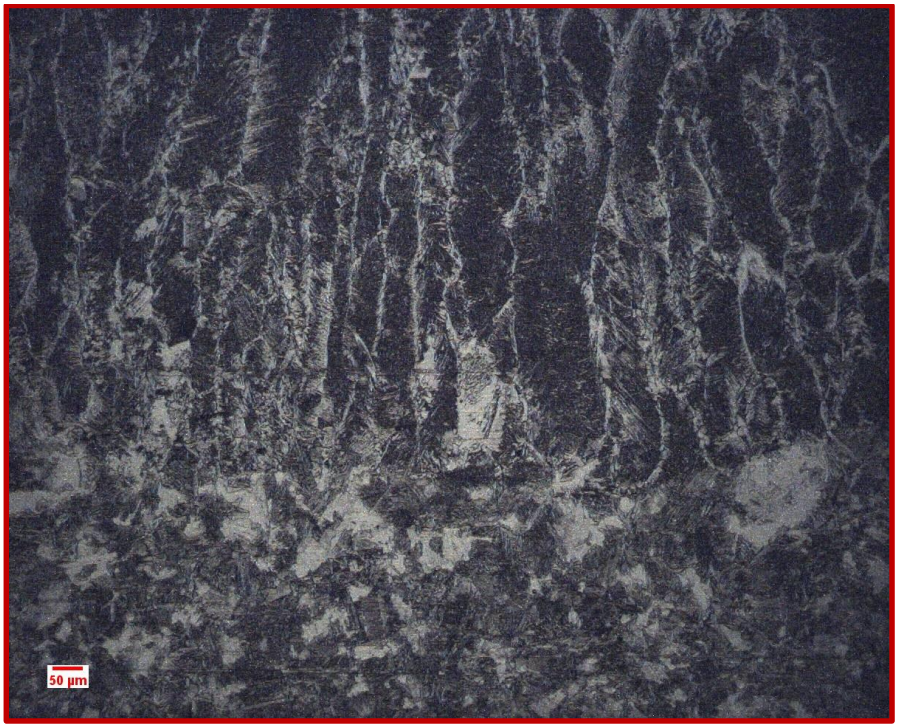

Figure 4.3: 38 HP S2

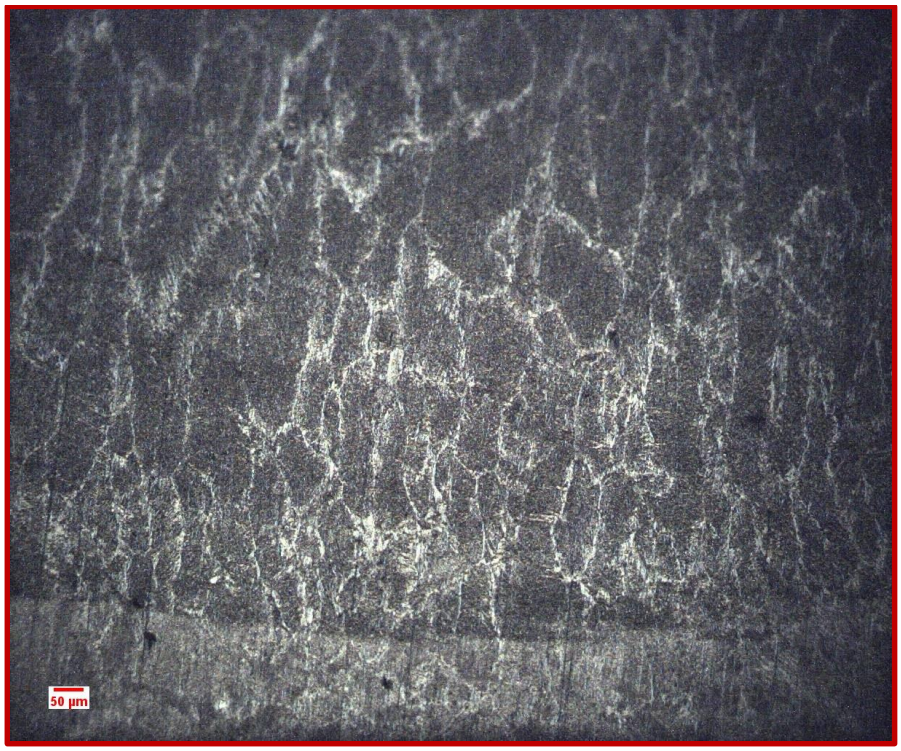

Figure 4.4: 56 LP S3

As can be seen from images Figure 4.1-4.4, there are visual changes in the grain formation and propagation under the influence of ultrasonic waves during rapid solidification. Some porosity is observed as shown in Figure 4.5, due to the ultrasonic vibration, which is confirmed by SEM t microstructure analysis.

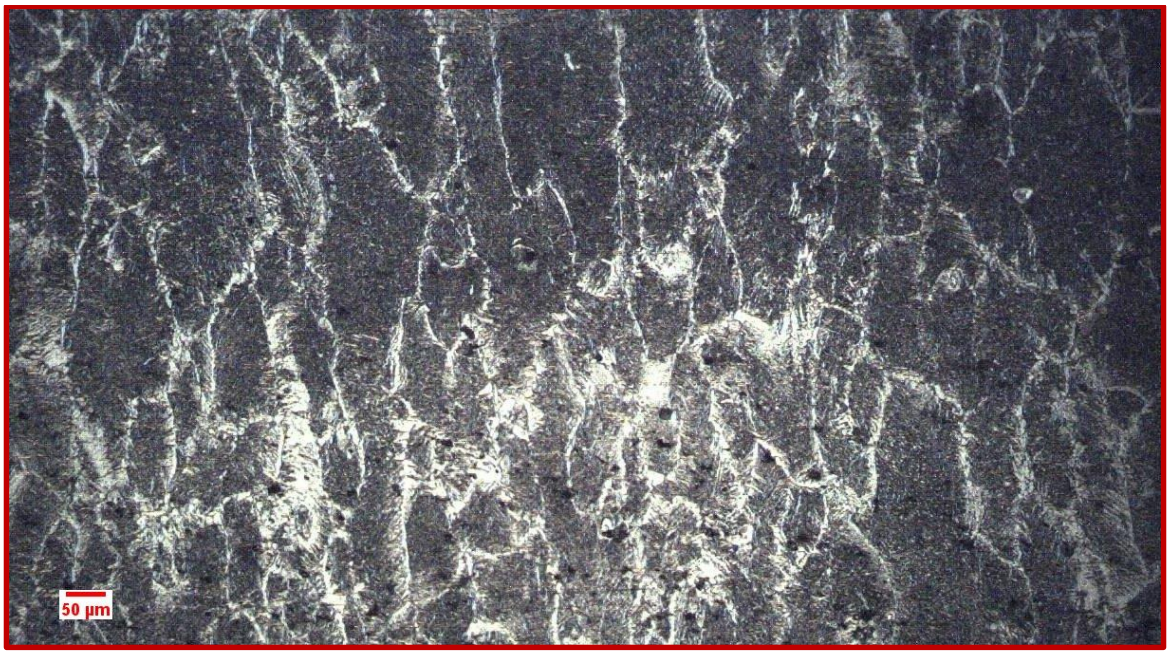

Figure 4.5: Porosity 38 HP S1

The microstructures were analyzed in ImageJ using the steps defined in Chapter 3 and the average area (µm^2), gain count information and standard deviation (SD) are presented in Table 4.3.

Table 4.3: Microstructure analysis results

Sample	Average area (µm^2)	SD	Grain count	SD
NV	314.565	28.422	344	114.858
LF LP	347.397	47.134	238	35.791
LF HP	343.734	38.052	341	135.709
MF LP	326.206	37.474	367	56.630
MF HP	281.113	37.361	523	107.685
HF LP	288.698	5.606	590	67.575
HF HP	296.424	24.612	462	67.174

From the analyzed data, Figures 4.6 and 4.7 show the effects of power and vibration on average grain size and grain count

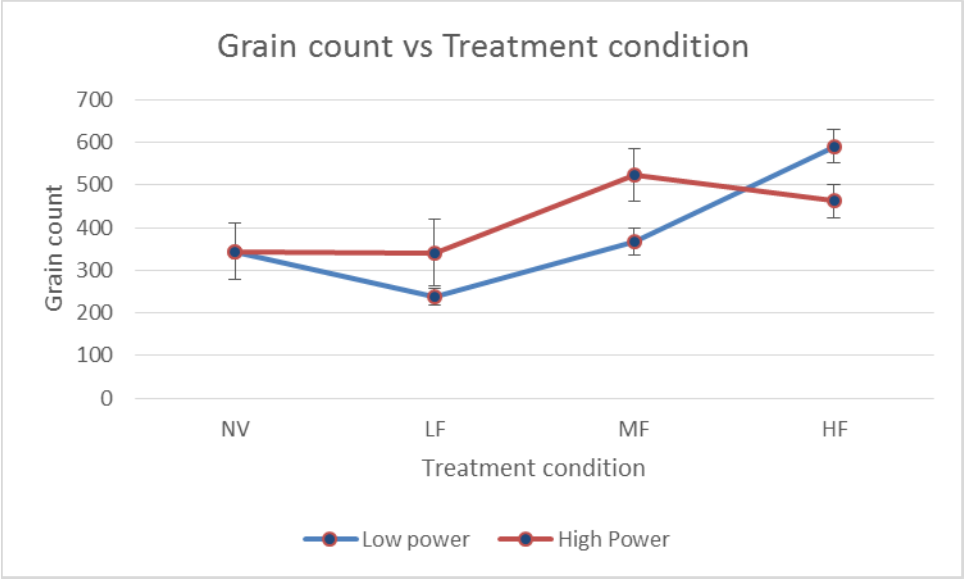

Figure 4.6: Grain count vs Treatment condition

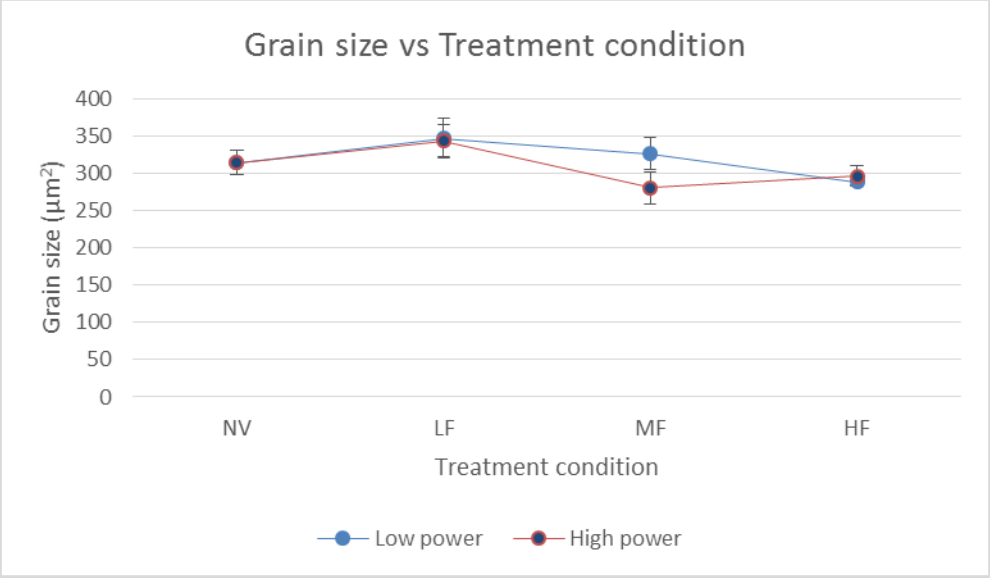

Figure 4.7: Average area (μm^2) vs Treatment condition

From Figure 4.6, it can be observed that, there is a pattern of increase in the grain count when ultrasonic vibration is applied when compared to the control. The highest grain count was identified for the HFLP (56 kHz 16.56 W) and the MFHP (38 kHz 19 W), indicating that greater disruption in columnar grain structure is achieved through increase in frequency and power. It is interesting to observe that the grain count has reduced for LFLP (20 kHz 3 W) indicating refinement instead of disruption, which can be attributed to the increase in the average grain size as shown in Figure 4.7. In addition, Figure 4.7 shows that there is a correlation between disrupting number of grains and refinement of average grain size (which decreases).

Two factor ANOVA analysis with replication was performed on the obtained data to determine the effect of power and frequency on the average grain area and the analysis is shown in Table 4.4

Table 4.4: ANOVA results- Grain area

ANOVA- Grain area (μm^2)						
Source of Variation	***SS***	***df***	***MS***	***F***	***P-value***	***F crit***
Power	4282.76	6	713.79	1.26	0.305976764	2.45
Frequency	831739.63	1	831739.63	1471.28	9.46608E-26	4.20
Power and Frequency	15856.82	6	2642.80	4.67	0.002067985	2.45
Within	15828.91	28	565.32			
Total	**867708.1248**	**41**				

At 95% confidence interval, it can be observed from the analysis that there is no effect of power on the average grain size as the P-value > 0.05 and that frequency has a major impact on the grain area when compared to the power and both frequency and power combined has an impact on average grain area.

Another ANOVA two factor analysis with replication was performed to determine the impact of power and frequency on the count of the number of grains and the results are shown in Table 4.5.

Table 4.5: ANOVA results- Grain count

ANOVA- Grain count						
Source of Variation	***SS***	***df***	***MS***	***F***	***P-value***	***F crit***
Power	169792.90	6	28298.82	6.98	0.000129731	2.45
Frequency	1490470.10	1	1490470.10	367.55	1.22663E-17	4.20
Power and Frequency	103664.90	6	17277.48	4.26	0.003594787	2.45
Within	113544.00	28	4055.14			
Total	**1877471.905**	**41**				

It can be observed from the ANOVA analysis results that at 95% confidence interval, power and frequency as well as their interaction have significant effect on the number of grains.

4.3. Microhardness Analysis:

The Vickers hardness test described in Chapter 3 was performed on all the samples at the heat affected zone (HAZ) and weld bead (WB) using Nanovea micro hardness testing machine and the loading curve is as shown in Figure 4.9 and the results are shown in Table 4.6.

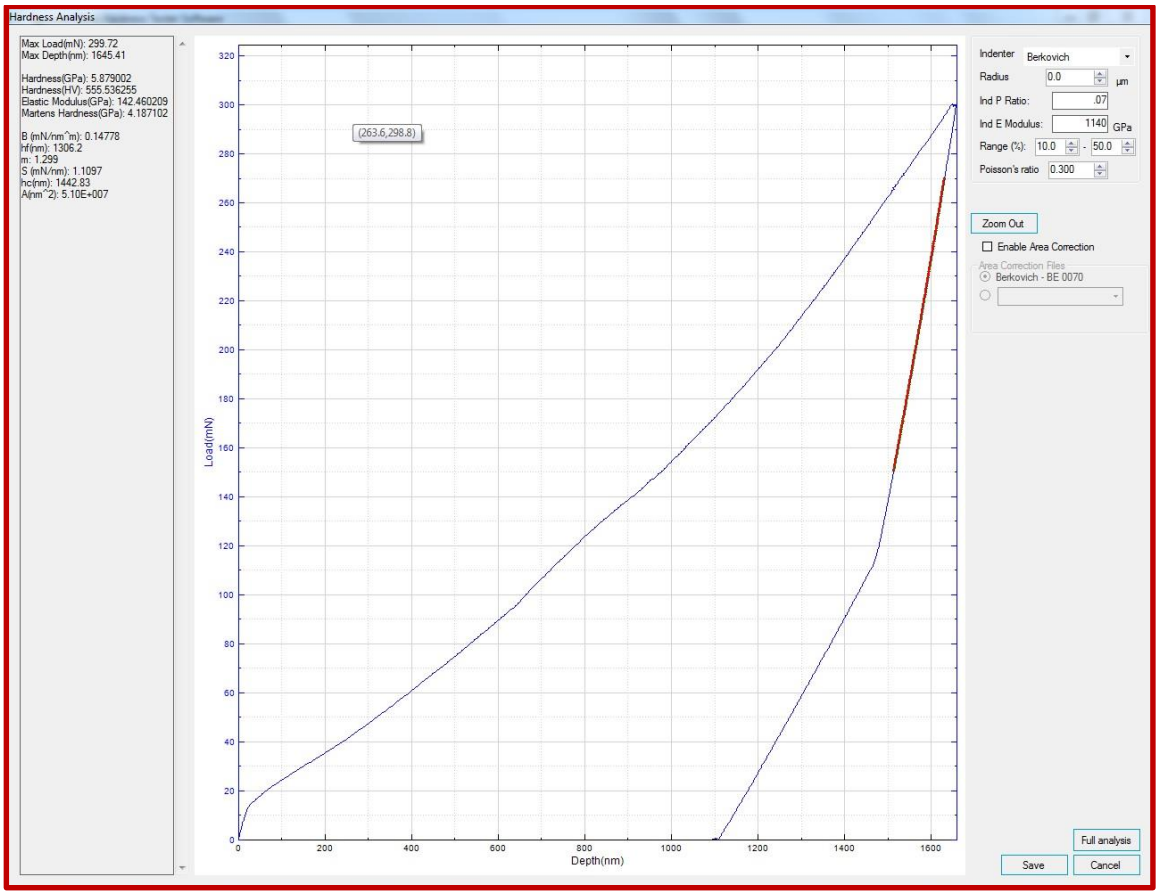

Figure 4.8: Load curve NV

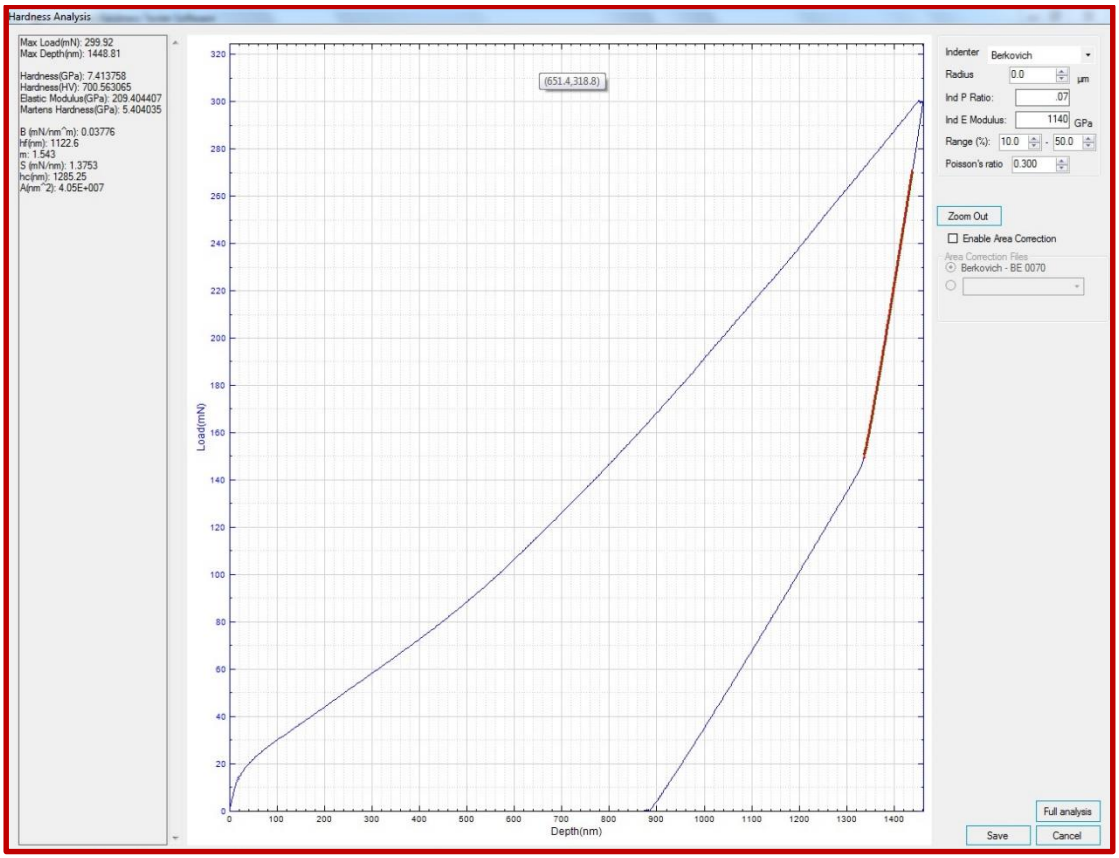

Figure 4.9: Load curve MF LP

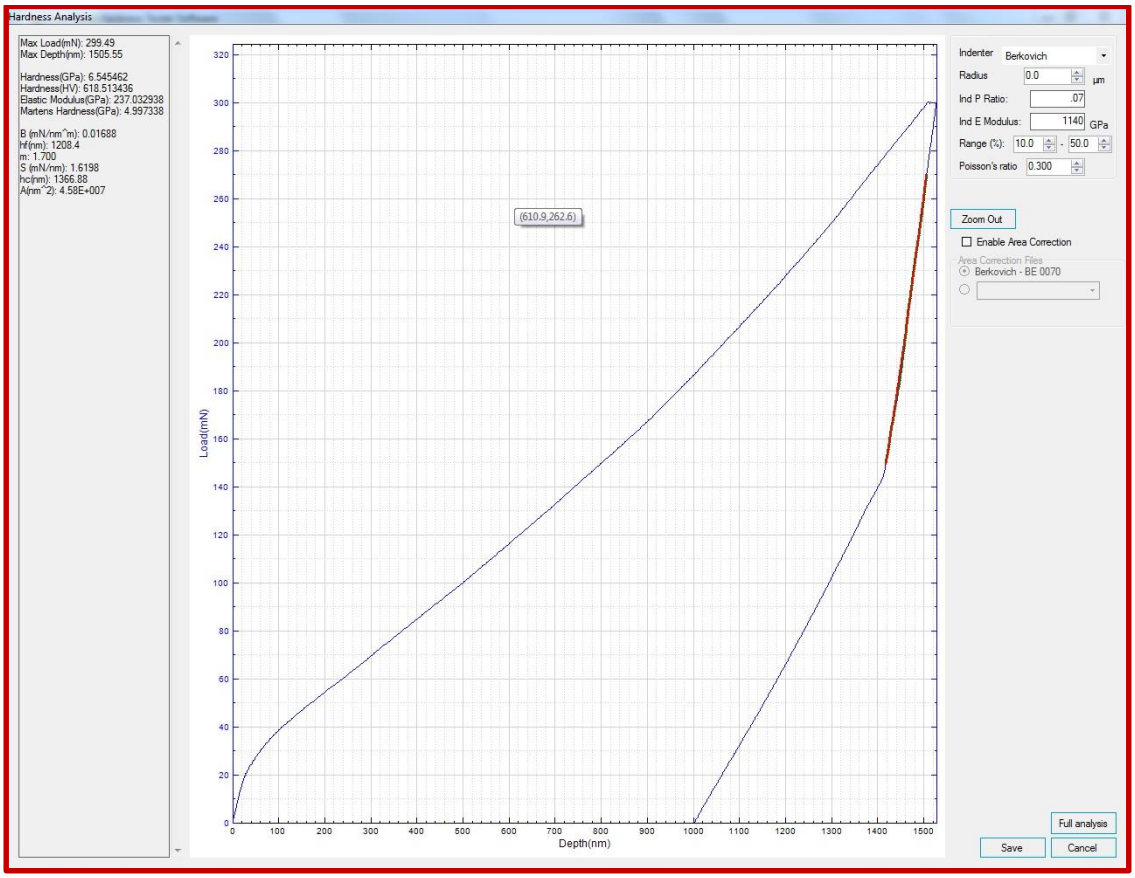

Figure 4.10: Load curve HF LP

The highlighted region (red) indicates the elastic unloading area and is used for calculating hardness and Young's modulus. The load curve shows a 300 mN load being applied on the region of interest at a loading and unloading rate of 160 mN/min, with a creep for 15 sec. The difference in the depth of penetration in Figures 4.9-4.11 is of interest.

Table 4.6: Microhardness test results

Sample	Hardness at HAZ (GPa)	SD	Hardness at WB (GPa)	SD	YM at HAZ (GPa)	SD	YM at WB (GPa)	SD
NV	5.148	1.231	7.479	1.458	161.730	19.298	198.984	45.461
LF LP	5.903	1.088	7.906	0.159	217.514	22.890	304.759	39.785
LF HP	5.322	1.067	7.046	0.332	234.971	32.506	250.819	69.983
MF LP	6.288	0.928	6.011	0.197	215.233	19.483	223.206	56.500
MF HP	5.296	1.209	7.212	1.734	251.767	43.073	309.820	98.018
HF LP	5.621	0.650	7.060	1.238	318.209	73.084	223.658	39.163
HF HP	5.607	0.585	8.728	1.453	236.664	72.737	252.218	62.656

Figures 4.12 - 4.14 presents the effects of ultrasonic vibration on Hardness.

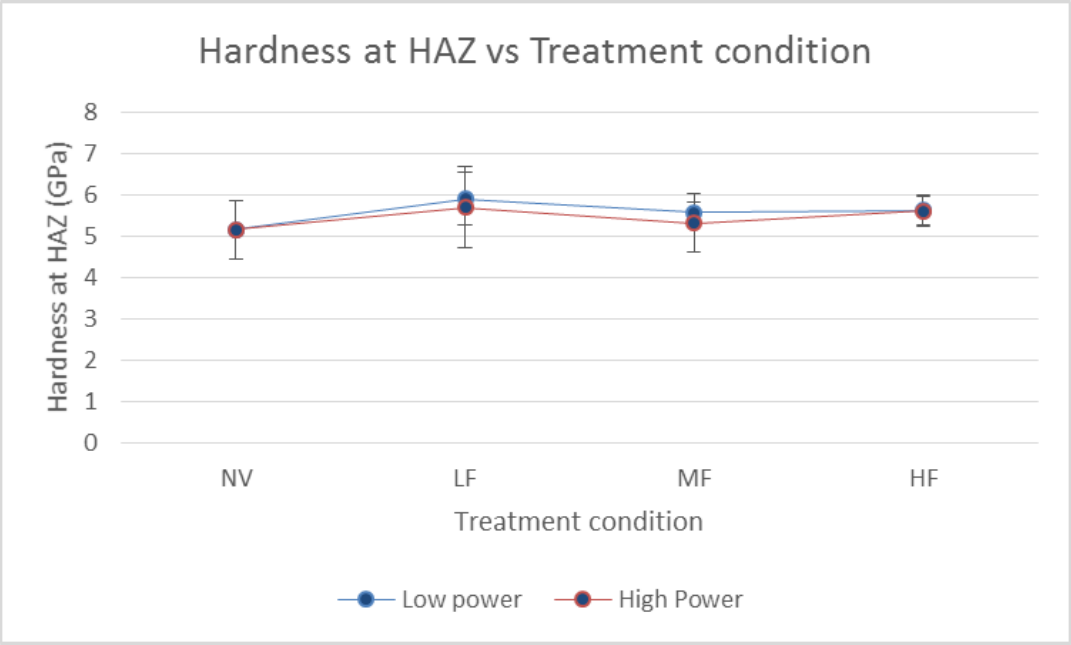

Figure 4.11: Hardness at HAZ (GPa) vs Treatment condition

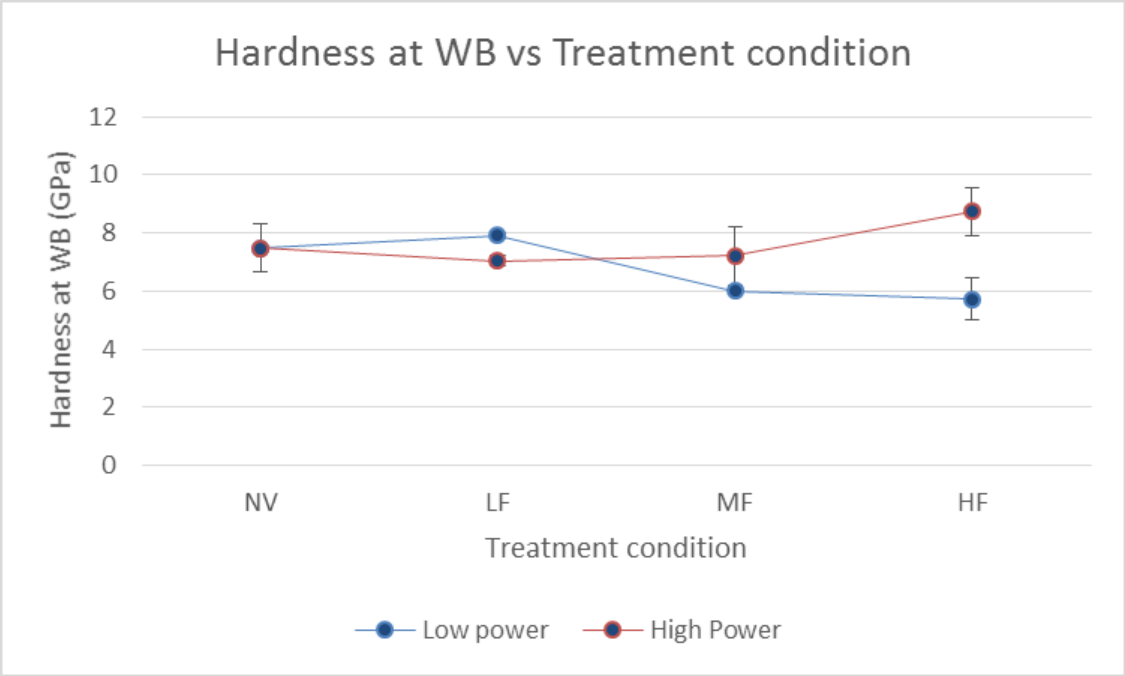

Figure 4.12: Hardness at WB (GPa) vs Treatment condition

It can be observed that there is an increase in the hardness due to ultrasonic vibration in both HAZ and weld-bead. In the case of HAZ, the LF HP (20 kHz 4.57 W) condition has higher hardness followed by the LF LP (20 kHz 3 W). In the case of weld bead, the HF HP (56 kHz 30.83 W) condition has greater hardness.

Two factor ANOVA analysis with replication is performed to determine the effect of both frequency and power on hardness at HAZ and the results are shown in Table 4.7.

Table 4.7: ANOVA results- Hardness at HAZ

ANOVA- Hardness at HAZ						
Source of Variation	*SS*	*df*	*MS*	*F*	*P-value*	*F crit*
Power	3853.3791	6	642.2298499	1298.217654	6.81845E-33	2.445259395
Frequency	7639.576281	1	7639.576281	15442.80883	6.05176E-40	4.195971819
Power & Frequency	3750.581385	6	625.0968976	1263.584724	9.94061E-33	2.445259395
Within	13.851634	28	0.494701214			
Total	15257.3884	41				

It is observed from the results of ANOVA analysis that frequency, power and their interaction have a major impact on the hardness at HAZ.

Another ANOVA two factor analysis with replication is used to determine the effect of power and frequency on the hardness at WB and the results are shown in Table 4.8.

Table 4.8: ANOVA results- Hardness at WB

ANOVA- Hardness at WB						
Source of Variation	*SS*	*df*	*MS*	*F*	*P-value*	*F crit*
Power	3837.203809	6	639.5339682	1000.380888	2.57568E-31	2.445259395
Frequency	6679.895372	1	6679.895372	10448.92061	1.41895E-37	4.195971819
Power & Frequency	3776.583238	6	629.4305396	984.5767596	3.21513E-31	2.445259395
Within	17.90013317	28	0.63929047			
Total	14311.58255	41				

Again it is observed from the results of ANOVA analysis that frequency, power, as well as their interactions have a major impact on the hardness of the weld bead.

Figures 4.15 - 4.17 presents the effects of ultrasonic vibration on Young's modulus.

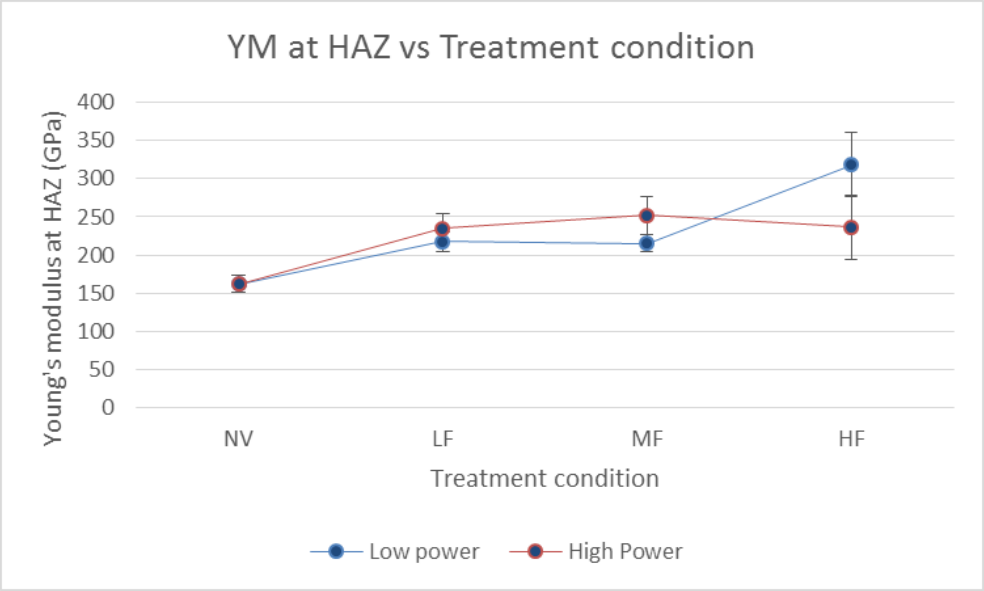

Figure 4.13: Young's modulus (GPa) vs Treatment condition at HAZ

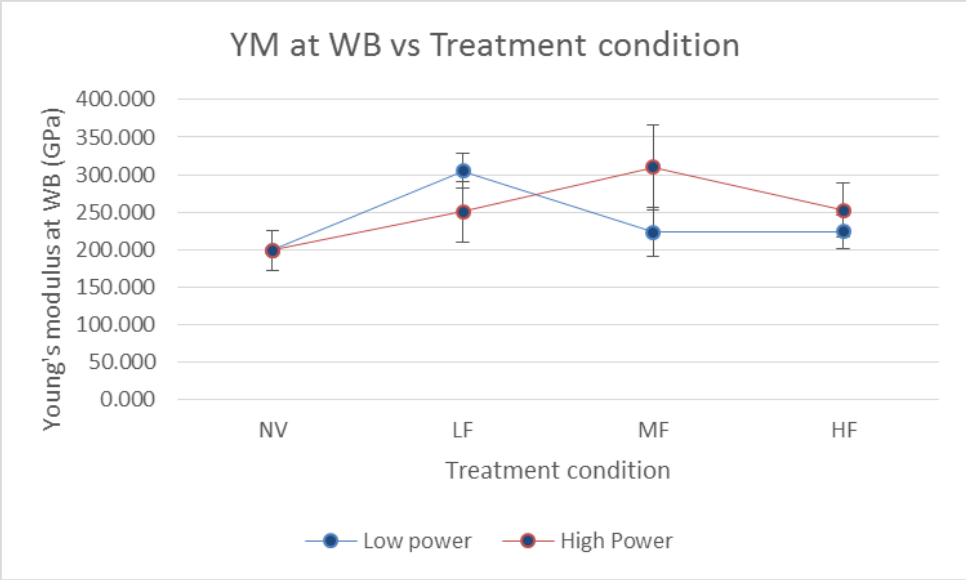

Figure 4.14: Young's modulus vs Treatment condition at WB

The plots indicate that there is a significant impact of the ultrasonic waves on the Young's modulus of the samples. In order to confirm this, a two factor ANOVA analysis with replication is performed to determine the effect of both frequency and power on Young's modulus at HAZ and the results are shown in Table 4.9.

Table 4.9: ANOVA results- Young's modulus at HAZ

ANOVA						
Source of Variation	***SS***	***df***	***MS***	***F***	***P-value***	***F crit***
Power	37429.27834	6	6238.213056	5.893067767	0.000449937	2.445259395
Frequency	424866.013	1	424866.013	401.3592008	3.88012E-18	4.195971819
Power & Frequency	9956.002338	6	1659.333723	1.567526788	0.193542582	2.445259395
Within	29639.90446	28	1058.568016			
Total	501891.1982	41				

It can be observed that frequency and power individually had an impact on the Young's modulus at HAZ, while the combination of both had no effect.

Another ANOVA two factor analysis with replication is used to determine the effect of power and frequency on the Young's modulus at WB and the results are shown in Table 4.10.

Table 4.10: ANOVA results- Young's modulus at WB

ANOVA- Young's modulus at WB						
Source of Variation	***SS***	***df***	***MS***	***F***	***P-value***	***F crit***
Power	21388.56181	6	3564.760301	1.861743767	0.123066489	2.445259395
Frequency	505211.1974	1	505211.1974	263.853308	8.76535E-16	4.195971819
Power & Frequency	17926.17895	6	2987.696492	1.560364471	0.195670135	2.445259395
Within	53612.79581	28	1914.742707			
Total	598138.7339	41				

It can be observed that only frequency had an impact on the Young's modulus at WB and neither power alone nor the combination of power and frequency had an effect.

The obtained results are in agreement with findings of Longbiao He and G. I Eskin and B.G. Eskin [4-1 and 4-2] who studied the effects of ultrasonic generation by modulated welding arc for grain structure refinement.

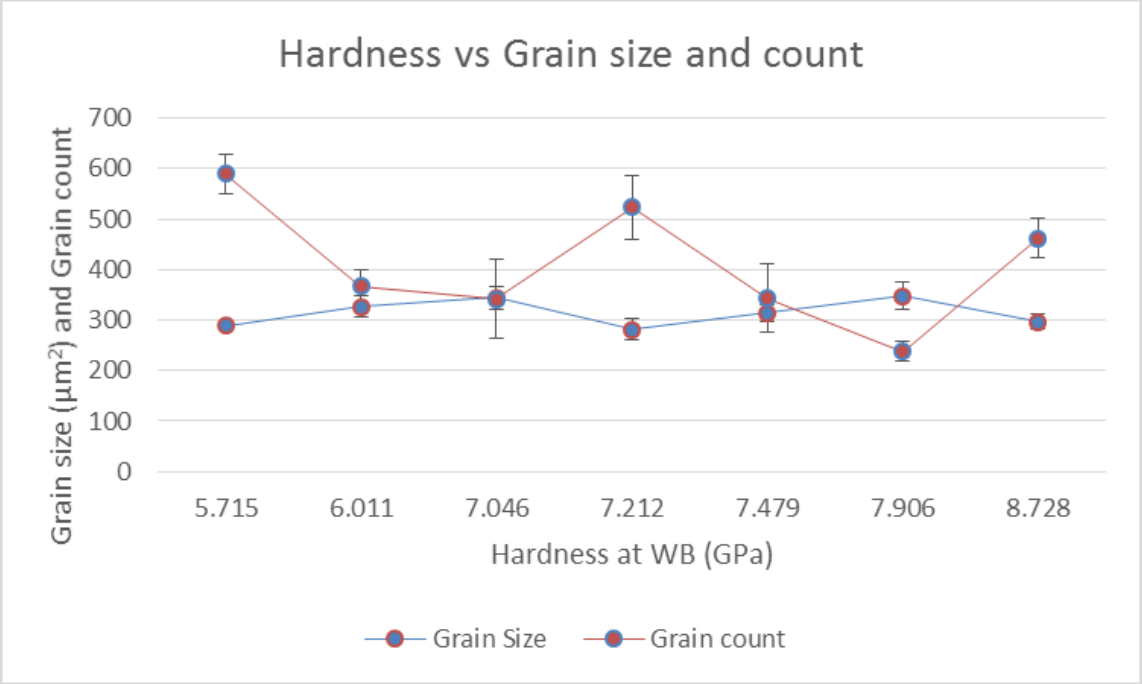

Figure 4.15: Hardness vs Grain size and count

4.4. Summary:

In summary this chapter presented results from power calculations, microstructure analysis and microhardness testing. Through ANOVA analysis it was found that power of ultrasonic vibration did not impact average grain area and Young's modulus of WB, but had a significant impact on grain count and hardness at both HAZ and WB and young's modulus at HAZ. On the other hand, frequency had an impact on average grain area, grain count, hardness at HAZ and WB and also Young's modulus at HAZ and WB. It was also found that there is a significant impact of the interaction of power and

frequency on the microstructures and hardness response variables that requires further analysis (through modeling and experimentation).

References:

4-1 Longbiao He, Minsheng Wu, Luming Li, and Hongwei Hao, 2009, "Ultrasonic generation by exciting electric arc: A tool for grain refinement in welding process", Journal of Manufacturing Processes 11, 38–44

4-2 G.I Eskin, D.G. Eskin , 2003, "Production of natural and synthesized aluminum-based composite materials with the aid of ultrasonic (cavitation) treatment of melt", Ultrasonics Sonochemistry 10, 297–301

Chapter 5: Conclusion and Future work

This study provided a broad introduction to manufacturing and its evolution from the traditional practices to Additive manufacturing (AM), concepts of microstructures, rapid solidification, ultrasound and power ultrasonics, transducers and welding in chapter 1.

In Chapter 2, the literature review and current findings on disruption of columnar grains, a review of literature focused on ultrasonic application for porosity reduction and grain structure refinement, modeling efforts of ultrasonic propagation, rapid solidification and applications of ultrasonics in Additive Manufacturing (AM) were presented. Also, various studies on the behavior of columnar grains during rapid solidification and under the influence of ultrasonics and the application of ultrasonics in industrial grade LENS technology were presented. Since this experiment is related to manufacturing and processing of materials, ultrasonic transducers which are applied for microstructure refinement and porosity control were emphasized.

In Chapter 3, the experimental setup and methodology used in this research were discussed. The experimental setup involved a low cost metal 3D printer originally developed by Joshua M. Pearce and his team at Michigan Technological University and an ultrasonic transducer setup developed in Center for Innovation in Additive Manufacturing (CIAM) at Youngstown State University. The ultrasonic setup to induce vibration during deposition includes a 50 kHz ultrasonic transducer, digital multimeters, a driver for ultrasonic transducer and a transformer to vary the power input to the transducer. The materials involved in the construction of each component were also explained in this chapter. Also experimental techniques used in this study like the sample

preparation using Struers grinding and polishing wheels, etching with 2% Nital, optical microscopy for taking microstructure images, image processing using ImageJ and microhardness testing using Nanovea micro hardness testing machine were presented. The obtained results, were analyzed using ANOVA analysis for determining the statistical integrity of the data and statistically determine which of the parameters: power or frequency had a major impact on the hardness and microstructure.

In Chapter 4, the resulting data obtained from ImageJ and Nanovea hardness testing machine were presented and analyzed. Power calculations, on energy input through vibration is determined along with the design of experiments; microstructure analysis; and microhardness analysis. ANOVA analysis was used in order to find the statistical impact of vibration parameters and resulting microhardness/strength. Also, a summary of the results and observations are presented. Though power had an impact on the increasing the number of grains, hardness at weld bead and young's modulus at HAZ, it was found that the frequency and interaction between power and frequency had statistically significant impact on grain count, grain size, hardness at both WB and HAZ, and the Young's modulus at both WB and HAZ.

In summary, following are the research contributions from this study:

- Fabrication of a control system for ultrasonic transducer and integration into an open source low cost metal printer.
- Analysis of impact of ultrasonic vibration on grain count and average grain size, which was further validated by hardness testing at both weld bead and HAZ.

Future Work

The future direction for this work should involve study on:

1) Modeling of the propagation of ultrasonic waves during rapid solidification using FEA tool (due to the transient nature of solidifying metal from liquid to solid).
2) Employing a broader range power and frequency that would lead to empirical modeling of the process.
3) Secondary impact on rapid solidification (porosity, phase distribution, etc.)
4) Influence of direction of applied vibration and interaction of vibration from different directions.
5) Influence of wave format (e.g. sine vs. pulse) on the process.
6) Correlating displacement on the substrate due to vibration and the grain structures

Appendix I: Experimental data

Frequency (khz)	Power (W)	Grain size (μm^2)	Average Grain Size ($\mu m2$)	SD	Grain count	Average Grain count	SD	Hardness-HAZ (Gpa)	Average Hardness at HAZ (Gpa)	SD	Hardness-WB (Gpa)	Average hardness at WB (Gpa)	SD	YM- HAZ (Gpa)	Average YM at HAZ (Gpa)	SD	YM-WB (Gpa)	Average YM at WB (Gpa)	SD
0	0	284.3			447			6.400			6.924			141.732			147.658		
0	0	340.69	314.565	28.422	220	344	114.858	3.940	5.148	1.231	6.381	7.479	1.458	163.216	161.730	19.298	215.111	198.984	45.461
0	0	318.704			364			5.105			9.133			180.242			234.184		
20	3	312.469			279			5.690			7.915			231.574			259.295		
20	3	401.009	347.397	47.134	213	238	35.791	7.083	5.903	1.088	7.743	7.906	0.159	229.866	217.514	22.890	333.198	304.759	39.785
20	3	328.714			222			4.938			8.061			191.101			321.785		
20	4.57	308.086			484			4.962			6.738			218.296			203.784		
20	4.57	339.313	343.734	38.052	325	341	135.709	7.642	5.695	1.703	7.002	7.046	0.332	272.431	234.971	32.506	331.243	250.819	69.983
20	4.57	383.804			214			4.482			7.398			214.187			217.431		
38	10.65	284.942			380			6.036			5.793			193.825			186.089		
38	10.65	335.555	326.206	37.474	416	367	56.630	5.512	5.570	0.440	6.177	6.011	0.197	219.949	215.233	19.483	195.299	223.206	56.500
38	10.65	358.12			305			5.162			6.062			231.925			288.230		
38	19	238.474			637			5.431			5.604			215.055			196.648		
38	19	308.116	281.113	37.361	423	523	107.685	4.054	5.318	1.211	6.984	7.212	1.734	241.064	251.767	43.073	365.217	309.820	98.018
38	19	296.75			509			6.469			9.049			299.183			367.597		
56	16.56	286.869			668			6.081			5.792			234.577			244.722		
56	16.56	294.99	288.698	5.606	558	590	67.575	5.904	5.621	0.650	6.926	5.715	1.252	369.799	318.209	73.084	178.472	223.658	39.163
56	16.56	284.234			545			4.877			4.426			350.252			247.781		
56	30.83	280.402			516			6.163			10.138			169.676			213.705		
56	30.83	284.107	296.424	24.612	387	462	67.174	4.997	5.607	0.585	8.812	8.728	1.453	226.281	236.664	72.737	218.435	252.218	62.656
56	30.83	324.762			484			5.663			7.235			314.035			324.516		

Appendix II: Instructions for Printer and Transducer control

Printer control:

1. Connect the USB cable from the Arduino motherboard to the computer.
2. Turn ON the 12V power supply.
3. Launch Repetier application
4. Connect to the printer by pressing the connect button in Repetier
5. Select home from the manual control tab
6. Type the Gcode or select the object and slice to generate the Gcode

Transducer control:

1. Connect the digital Multimeters, transducer driver, transformer to the transducer
2. Connect the frequency modulator and input the 0-5V and the required frequency
3. Apply Glycerin between the polystyrene horn and the piezoelectric element
4. Turn ON the driver switch and the transducer switch and adjust the power input accordingly.